Charge and spin currents in ferromagnetic Josephson junctions

Klaus Halterman,[1,*] Oriol T. Valls,[2,†] and Chien-Te Wu[3,‡]
[1]*Michelson Lab, Physics Division, Naval Air Warfare Center, China Lake, California 93555, USA*
[2]*School of Physics and Astronomy, University of Minnesota, Minneapolis, Minnesota 55455, USA*
[3]*The James Franck Institute, The University of Chicago, Chicago, Illinois, 60637, USA*
(Received 22 May 2015; revised manuscript received 28 August 2015; published 16 November 2015)

We determine, using a self-consistent method, the charge and spin currents in ballistic Josephson junctions consisting of several ferromagnetic (F) layers sandwiched between superconducting (S) electrodes (*SFS*-type junctions). When there are two F layers, we also consider the experimentally relevant configuration where a normal (N) nonmagnetic spacer layer separates them. We study the current-phase relationships as functions of geometrical parameters that are accessible experimentally including particularly the angles that characterize the relative orientation of the magnetization in the F layers. Our self-consistent method ensures that the proper charge conservation laws are satisfied, and that important proximity effects are fully and properly accounted for. We find that as we vary the phase difference $\Delta\varphi$ between the two outer S electrodes, multiple harmonics in the current-phase relations emerge, the extent of which depends on the interface scattering strength and on the relative F layer widths and magnetization orientations. By manipulating the relative F layer magnetization orientations, we find that the charge supercurrent can reverse directions or vanish altogether. These findings are discussed in the context of the generation and long-range nature of triplet pair correlation within these structures. We also investigate the spin currents and associated spin-transfer torques throughout the entire junction regions. For noncollinear relative magnetizations, the nonconserved spin currents in a given F region give rise to net torques that can switch directions at particular magnetic configurations or $\Delta\varphi$ values. The details of the spin current behavior are shown to depend strongly on the degree of magnetic inhomogeneity in the system, including the number of F layers and the relative widths of the F and N layers.

DOI: 10.1103/PhysRevB.92.174516 PACS number(s): 74.45.+c, 74.25.Bt, 74.78.Fk

I. INTRODUCTION

When a phase difference $\Delta\varphi$ exists between two superconductor (S) electrodes separated by a nonsuperconducting material in a Josephson junction, the corresponding charge supercurrent is directly controllable via $\Delta\varphi$. Motivated by the interplay between ferromagnetism and superconductivity, researchers are also interested in the dc Josephson effect in superconducting junctions that contain a central ferromagnet (F) region, which in turn can give rise to an additional spin degree of freedom. More specifically, this kind of Josephson effect provides a venue for the study of spin currents that can be manipulated in cryogenic spintronic systems [1–3]. Besides numerous practical applications [4] involving these *SFS*-based Josephson junctions, it is found that novel and interesting phenomena can arise. For example, the realization of a π state [4–8], where the ground state of the system corresponds to $\Delta\phi = \pi$ across the junction. Moreover, if the ferromagnet region consists of at least two F layers that each have a uniform magnetization (e.g., a *SFFS* structure), manipulation of the angle between the magnetization vectors can serve to generate long-range triplet supercurrents [9–14] in addition to the ordinary singlet ones. Additional control of the magnetic state can also occur from the spatially varying spin current within the F layers of the junction, causing mutual torques to act on their respective magnetic moments. Therefore, *SFS*-based junctions that contain multiple F layers present many opportunities for controlling the charge and spin currents, and their influence on the magnetization in terms of the torque they produce.

Besides these potential applications, it is also of fundamental importance to understand the basic physics of the interplay between spin and charge currents and the long-range triplet pairing associated with the supercurrents. For these purposes, we consider in this paper nanoscale *SFS* Josephson junctions, where the F region contains multiple layers: *SFFS* spin valves consisting of two metallic ferromagnets separated by a nonmagnetic normal-metal spacer, and trilayer *SFFFS* junctions. In each case, a supercurrent is established via a phase difference $\Delta\varphi$ between the S terminals. Interest in superconducting spin valves has recently extended to the use of strong, even half-metallic, ferromagnets [3,15,16]. Because the characteristic lengths associated with proximity effects in a moderate to strong magnet are comparable to the Fermi wavelength, a quasiclassical approach in the diffusive limit is usually not suitable [17] and a microscopic theory is necessary. Furthermore, recent experimental evidence [18–20] strongly suggests the ballistic regime is the relevant one: as demonstrated in Refs. [19,20], the numerical solutions of the Bogoliubov–de Gennes (BdG) equations [21] in the clean limit clearly agree in quantitative detail with experimental data. Hence, in this work we consider the *ballistic* limit and adopt a self-consistent BdG calculation that permits us to properly take into account the microscopic origin of the proximity effects in the Andreev reflections. Our results, obtained from a fully self-consistent microscopic approach, are therefore in previously unexplored regimes.

*klaus.halterman@navy.mil
†Also at Minnesota Supercomputer Institute, University of Minnesota, Minneapolis, Minnesota 55455; otvalls@umn.edu
‡Also at School of Physics and Astronomy, University of Minnesota, Minneapolis, Minnesota 55455; chientewu@uchicago.edu

Using this framework, we find that the direction of charge supercurrents can be reversed by adjusting the relative magnetic orientations of F layers. We demonstrate that this phenomenon is connected with both the π-state Josephson junction and with the triplet correlations. It has long been known [19,20,22] that experimental results depend crucially on many parameters. Because of this, wide parameter ranges are considered here, including F layer widths, the strength of interfacial scattering, and the geometry of the different magnetic configurations. We illustrate how the spin currents locally satisfy the conservation law, and we also show that reversal of charge currents signals a phase change in the spin transport.

Although interest in the study of F/S multilayer structures has recently increased considerably, work on SFS Josephson junctions actually started long ago. The Josephson and critical current oscillations were found to occur as a function of the ferromagnet exchange field [23,24] and the thickness of the magnet [24]. An essential principle behind many of these important phenomena is the damped oscillatory nature of the singlet Cooper pairs in the ferromagnetic regions, and the associated phase shift in the superconducting order parameter. Due to the intrinsic exchange field in the ferromagnet regions, electrons of Cooper pairs with spin up (down) decrease (increase) their kinetic energy and the Cooper pairs acquire a nonzero center-of-mass momentum. It further leads to an oscillatory order parameter in the F regions [25]. Owing to this oscillatory nature, not only the Josephson critical current but also the superconducting critical temperatures oscillate as a function of exchange field and thickness of magnets. Josephson junctions of the π type can also be realized by using this principle by adjusting either the exchange field, the magnet width, or both [6,26,27]. The proximity effects between the S and F regions thus give rise to phenomena [17,25,28,29] that subsequently play crucial roles in the charge and spin currents that may be manipulated in low-temperature nanoscale devices, including nonvolatile memory elements, where the dissipationless nature of the supercurrent flow offers reduced energy loss and Joule heating.

In equilibrium, singlet Cooper pairs carry no net spin, hence, any spin current in the system either flows only within the ferromagnets due to their exchange interaction, or it flows by means of induced equal-spin triplet correlations, where the Cooper pairs have a net spin of $m = \pm 1$ on the spin quantization axis and they can reside in both S and F regions. The generation of long-range triplet proximity effects in superconducting heterostructures with magnetic inhomogeneity has been both theoretically predicted and experimentally confirmed: by introducing magnetic inhomogeneity, e.g., inclusion of an additional magnet with misaligned exchange field, the Hamiltonian no longer commutes with the total spin operator and equal-spin triplet correlations can then be induced [14,30,31]. Due to the imbalance between majority and minority spins in a ferromagnet, conventional singlet superconducting correlations do not survive for long once inside the magnetic region. However, Cooper pairs with electrons that carry the same spin are not subject to paramagnetic pair breaking and can in principle propagate for large distances inside the ferromagnet, limited only by coherence breaking processes [11,14,30,31]. Such equal-spin triplet correlations thus play an important role in Josephson junctions with inhomogeneous ferromagnets [11,32,33]. Indeed, it has been reported experimentally that with the presence of magnetic inhomogeneity, the Josephson critical current decays much more slowly with increases in the F layer thicknesses [34,35], as compared to junctions with homogeneous magnetization. One of the simplest ways to introduce magnetic inhomogeneity in a Josephson junction is through the insertion of bilayer or trilayer of uniformly magnetized ferromagnets. Experimentally, this has the advantages of reproducibility and easy manipulation of the relative exchange field orientation. These structures also provide direct evidence of triplet correlations [19,36–38]. Recently, long-range coherent transport of triplet pairs was studied in double-magnet SF_1F_2S junctions [2,39], further demonstrating that it is not always necessary to have a trilayer [40] ferromagnet structure of misaligned ferromagnets to generate equal-spin triplet components to the supercurrent. This finding was in agreement with the long-range phenomena found in a similar structure [12] with asymmetric widths [12] and orthogonal exchange fields. The behavior of the triplet amplitude is often anticorrelated [38] to that of the critical temperature and associated singlet correlations, suggesting singlet-to-triplet conversion.

The oscillatory and long-range pair correlations also lead to new behaviors in the current-phase relations (CPRs) in SFS juncitons [4,9,41] with a nontrivial magnetic structure. The CPR can in general contain not only the first harmonic but also higher-order harmonics, i.e., $I(\Delta\varphi) \approx I_1 \sin(\Delta\varphi) + I_2 \sin(2\Delta\varphi)$. The appearance of additional harmonics in the current-phase relation has also been discussed in the diffusive and clean regimes for ferromagnetic Josephson junction structures [17,32,42,43]. In conventional Josephson junctions without any magnetic interaction, the magnitude of I_2 is much smaller than that of I_1. However, in SFS Josephson junctions, near a 0 to π phase transition, the roles of the first harmonic and the second harmonic can be reversed, and the CPR can be largely dominated by the second harmonic [42]. In this regime, both $\Delta\varphi = 0$ and π states can be stable or metastable, and they can coexist. The physical origins of the second- and higher-order harmonics are believed to lie in the long-ranged triplet component of the supercurrent. In this regard, within the vicinity of the 0-π transitions, the triplet correlations can be tuned accordingly. Since the first harmonic is suppressed due to the supercurrent flow reversing direction, the higher-order harmonics are revealed at the 0-π transition point. The influence of interface scattering on the higher-order harmonics was investigated in the quasiclassical clean limit [44] and experimentally detected [45]. The measured supercurrent at the 0-π transition point [8] was attributed to the presence of higher harmonics. Subsequent work with ferromagnetic Josephson junctions demonstrated that the higher harmonics can naturally arise when varying the location of domain walls [46], and also in ballistic double-magnetic Josephson junctions, provided that the thicknesses of the magnetic layers are unequal [12]. Recently, evidence of higher harmonics has been observed in Josephson junctions with spin-dependent tunneling barriers [47].

The interaction of the spin current with the magnetization in layered ferromagnetic junctions with multiple ferromagnets has important consequences for memory technologies. Indeed,

storage of information bits depends on the precise relative orientation of the magnetizations in two F layers, where nonconserved spin currents reflect the mutual torque acting on the magnetic moments. The corresponding spin-transfer torque (STT) can also switch magnetizations when a spin-polarized electrical current flows perpendicular to the layers. Spin-transfer torque is known to occur in a very broad variety of materials, making it an attractive switching mechanism. For equilibrium spin currents, governed by spin-polarized Andreev bound states [48], tuning the supercurrent (via $\Delta\varphi$) directly influences the STT when varying the relative in-plane magnetization angle [49]. The direction of supercurrent flow, however, is not simply related to the direction of the induced torque that tends to align the magnetic moments. The triplet correlations generated in these types of Josephson junctions (with noncollinear relative magnetizations) can also induce spatial variations in the spin currents responsible for the mutual torques acting on the ferromagnets [13].

When considering superconducting proximity effects, it is important to make sure that the self-consistency condition for the pair potential $\Delta(x)$ is fulfilled [38] in order to obtain the correct physical picture. The self-consistency condition is often neglected in the literature [50] mainly because it is difficult to properly implement in the theoretical studies. As we will show in the Sec. II, a source term in the continuity equation for the charge currents usually arises when a non-self-consistent superconducting order parameter is used. More importantly, when the self-consistent condition is achieved, the free energies of these proximity-coupled systems are properly minimized. This concept is crucial especially when studying Josephson junctions since the superconducting proximity effects are the fundamental mechanism behind the nontrivial charge and spin currents that flow within these structures. Furthermore, when the solutions are self-consistent, the charge conservation law is satisfied by properly accounting for the proximity effects and transport properties for the charge current [51]. When magnetic inhomogeneity is present, the spin density is not conserved and STT can arise and interact with the charge-dependent quantities. Although there is no continuity equation for the spin density, since its gradients are nonzero, there is still a corresponding, and fundamental, conservation law that balances current gradients and the STT [38,52].

Above, we have discussed various physical phenomena associated with the magnetic inhomogeneity such as triplet correlations and the generations of STT and outlined the main goal of this work. The rest of the paper is organized as follows: We describe our method in Sec. II and derive conservation laws for both spin and charge currents. Our method is based on self-consistently solving the BdG equations. All important physical quantities, e.g., the magnetization, can be extracted or constructed from the self-consistent solutions. In Sec. III, we present a detailed study of the transport properties by considering a wide range of a number of material parameters. Finally, we conclude with our main findings in Sec. IV.

II. METHODS

The general method that we use in this paper is that of numerical diagonalization of the self-consistent Bogoliubov–de Gennes (BdG) equations. Since many aspects of this method have been extensively discussed in previous work [28,38,46,53], we will only include here a brief review of these points, as needed to make this paper understandable. We will discuss in more detail additional aspects needed for the transport calculations described in this work.

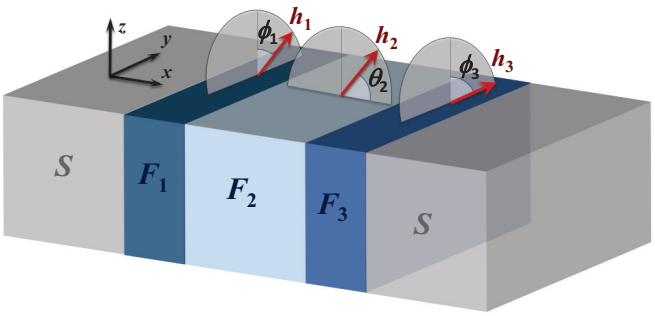

FIG. 1. (Color online) Schematic of the $SF_1F_2F_3$S Josephson junction considered in this paper. A generic configuration is shown, described by the in-plane magnetization angles ϕ_i and the out-of-plane angles θ_i ($i = 1,2,3$). The ferromagnetic exchange field $\boldsymbol{h}_i$ in each region is expressed as $\boldsymbol{h}_i = h_i(\cos\theta_i, \sin\theta_i \sin\phi_i, \sin\theta_i \cos\phi_i)$.

The derivation of the BdG equations for general magnetization configurations begins with the effective BCS Hamiltonian $\mathcal{H}$:

$$\mathcal{H} = \int d^3r\{\psi^\dagger(\boldsymbol{r})[\mathcal{H}_e - \boldsymbol{h}\cdot\boldsymbol{\sigma}]\psi(\boldsymbol{r}) + \Delta(\boldsymbol{r})\psi^\dagger_\uparrow(\boldsymbol{r})\psi^\dagger_\downarrow(\boldsymbol{r}) + \Delta^*(\boldsymbol{r})\psi_\downarrow(\boldsymbol{r})\psi_\uparrow(\boldsymbol{r})\}, \quad (1)$$

where $\psi(\boldsymbol{r}) \equiv (\psi_\uparrow, \psi_\downarrow)^T$ are the usual fermionic operators, $\mathcal{H}_e = -1/(2m)\nabla^2 - E_F + U(\boldsymbol{r})$, and $\boldsymbol{\sigma}$ denote the set of Pauli matrices. We describe the magnetism of the F layers by effective Stoner exchange fields $\boldsymbol{h}(\boldsymbol{r})$ which in our case have components in all (x,y,z) directions (see Fig. 1). The spin-independent scattering potential is denoted by $U(\boldsymbol{r})$, and $\Delta(\boldsymbol{r})$ is the pair potential.

To diagonalize the effective Hamiltonian, the field operators $\psi_\uparrow$ and $\psi_\downarrow$ are expanded [21] by means of a Bogoliubov transformation:

$$\psi_\uparrow(\boldsymbol{r}) = \sum_n (u_{n\uparrow}(\boldsymbol{r})\gamma_n - v^*_{n\uparrow}(\boldsymbol{r})\gamma^\dagger_n), \quad (2a)$$

$$\psi_\downarrow(\boldsymbol{r}) = \sum_n (u_{n\downarrow}(\boldsymbol{r})\gamma_n + v^*_{n\downarrow}(\boldsymbol{r})\gamma^\dagger_n), \quad (2b)$$

where $u_{n\alpha}$ and $v_{n\alpha}$ are the quasiparticle and quasihole amplitudes, which are chosen so that the Hamiltonian is diagonalized in terms of the fermionic γ_n operators. Therefore, $[\mathcal{H},\gamma_n] = -\epsilon_n\gamma_n$ and $[\mathcal{H},\gamma^\dagger_n] = \epsilon_n\gamma^\dagger_n$. Also, the thermal expectation values involving γ_n and $\gamma^\dagger_n$ are given by the usual Fermi functions f_n [54]. The anticommutation relations for ψ and $\psi^\dagger$ yield

$$[\psi_\uparrow(\boldsymbol{r}),\mathcal{H}] = (\mathcal{H}_e - h_z)\psi_\uparrow(\boldsymbol{r}) - [h_x - ih_y]\psi_\downarrow(\boldsymbol{r}) + \Delta(\boldsymbol{r})\psi^\dagger_\downarrow(\boldsymbol{r}), \quad (3a)$$

$$[\psi_\downarrow(\boldsymbol{r}),\mathcal{H}] = (\mathcal{H}_e + h_z)\psi_\downarrow(\boldsymbol{r}) - [h_x + ih_y]\psi_\uparrow(\boldsymbol{r}) - \Delta(\boldsymbol{r})\psi^\dagger_\uparrow(\boldsymbol{r}). \quad (3b)$$

It is convenient at this point to simplify to the quasi-one-dimensional (quasi-1D) geometry (Fig. 1) of our problem. Then, by inserting (2) into (3) and using the commutation relations, we obtain the general spin-dependent BdG equations for this geometry:

$$\begin{pmatrix} \mathcal{H}_0 - h_z & -h_x + ih_y & 0 & \Delta \\ -h_x - ih_y & \mathcal{H}_0 + h_z & \Delta & 0 \\ 0 & \Delta^* & -(\mathcal{H}_0 - h_z) & -h_x - ih_y \\ \Delta^* & 0 & -h_x + ih_y & -(\mathcal{H}_0 + h_z) \end{pmatrix} \begin{pmatrix} u_{n\uparrow}(x) \\ u_{n\downarrow}(x) \\ v_{n\uparrow}(x) \\ v_{n\downarrow}(x) \end{pmatrix} = \epsilon_n \begin{pmatrix} u_{n\uparrow}(x) \\ u_{n\downarrow}(x) \\ v_{n\uparrow}(x) \\ v_{n\downarrow}(x) \end{pmatrix}, \tag{4}$$

where ϵ_n are the quasiparticle energies, x is normal to the layers, which lie in the y-z plane (see Fig. 1), and $\Delta(x)$ is the pair potential, to be found self-consistently as explained below. Here, the single-particle Hamiltonian $\mathcal{H}_0$ is written

$$\mathcal{H}_0 = \frac{1}{2m}\left(-\frac{\partial^2}{\partial x^2} + k_y^2 + k_z^2\right) - E_F + U(x). \tag{5}$$

The components of the exchange field $\boldsymbol{h}$ in each of the F layers take the form

$$\boldsymbol{h}_i = h(\cos\theta_i, \sin\theta_i \sin\phi_i, \sin\theta_i \cos\phi_i), \tag{6}$$

where i denotes one of the magnetic layers. We will assume that the magnitude of the exchange field is the same in all magnetic layers, and that it vanishes elsewhere. The angles θ_i and ϕ_i will in general be taken to vary from layer to layer.

One obtains in the usual way [21] the self-consistency condition for the pair potential, using $\Delta(\boldsymbol{r}) = g\langle\psi_\downarrow(\boldsymbol{r})\psi_\uparrow(\boldsymbol{r})\rangle$. Here, g is the superconducting coupling constant, which vanishes in the non-S layers. In our geometry we find, after using the Bogoliubov transformation and making use of the appropriate averages such as $\langle\gamma_n^\dagger\gamma_n\rangle = f_n$, the pair potential can be expressed in terms of the quasiparticle amplitudes as an appropriate sum over states:

$$\Delta(x) = \frac{g}{2}{\sum_n}' [u_{n\uparrow}(x)v_{n\downarrow}^*(x) + u_{n\downarrow}(x)v_{n\uparrow}^*(x)]\tanh(\epsilon_n/2T), \tag{7}$$

where the prime on the sum indicates that only those states that have energies within a "Debye energy" ω_D are included.

The problem is then solved iteratively: the pair potential is initially taken to be Δ_0 in the first S layer and $\Delta_0\exp(i\Delta\varphi)$ in the second S layer, where Δ_0 is the initial guess of the magnitude for the pair amplitudes. The Hamiltonian is then numerically diagonalized and the new pair potential is found via Eq. (7). Iteration is continued until convergence. The details of the procedure, including the way to ensure, in the Josephson calculations, that the phase difference between the right and left ends of the sample remains $\Delta\varphi$, is explained in Appendix A.

Equilibrium and transport properties in the structures considered are strongly influenced by the existence of "odd" triplet pairs. The existence of such pairs is allowed by conservation laws since, unless all of the F layers have magnetizations along the same direction, the total spin of the Cooper pairs is not a conserved quantity. Because of the Pauli principle, these s-wave triplet pairs must have wave functions odd in frequency [55] or, equivalently [14,31], in time. Within the BdG framework, the time formulation is much more convenient. Accordingly, we will describe the triplet pair correlations via the following amplitude functions, in terms of the field operators

$$f_0(\boldsymbol{r},t) = \tfrac{1}{2}[\langle\psi_\uparrow(\boldsymbol{r},t)\psi_\downarrow(\boldsymbol{r},0)\rangle + \langle\psi_\downarrow(\boldsymbol{r},t)\psi_\uparrow(\boldsymbol{r},0)\rangle], \tag{8a}$$

$$f_1(\boldsymbol{r},t) = \tfrac{1}{2}[\langle\psi_\uparrow(\boldsymbol{r},t)\psi_\uparrow(\boldsymbol{r},0)\rangle - \langle\psi_\downarrow(\boldsymbol{r},t)\psi_\downarrow(\boldsymbol{r},0)\rangle]. \tag{8b}$$

Taking the quantization axis along the z direction, the triplet amplitudes f_0 and f_1 can be rewritten [14,31] in terms of the quasiparticle amplitudes

$$f_0 = 1/2\sum_n (g_n^{\uparrow\downarrow} - g_n^{\downarrow\uparrow})\zeta_n(t), \tag{9}$$

$$f_1 = 1/2\sum_n (g_n^{\uparrow\uparrow} + g_n^{\downarrow\downarrow})\zeta_n(t), \tag{10}$$

where $\zeta_n(t) \equiv \cos(\epsilon_n t) - i\sin(\epsilon_n t)\tanh(\epsilon_n/2T)$, and we define $g_n^{\sigma\sigma'} \equiv u_{n\sigma}v_{n\sigma'}^*$. It is sometimes necessary to evaluate the triplet amplitudes along a different spin axis. For example, one may wish to use the direction of the local magnetization (defined below) as the axis of quantization. To do so, one rotates the quantization axis so that it is aligned with the local magnetization direction using the spin rotation matrices discussed in Appendix B.

We will consider here spin currents, as well as charge currents. In our structures, spin transport is influenced by the leakage of magnetism out of the F layers and into the superconductors. This can be characterized by the local magnetization $\boldsymbol{m}(\boldsymbol{r})$:

$$\boldsymbol{m}(\boldsymbol{r}) = -\mu_B\langle\boldsymbol{\eta}(\boldsymbol{r})\rangle, \tag{11}$$

where $\boldsymbol{\eta}(\boldsymbol{r})$ is the spin density operator

$$\boldsymbol{\eta}(\boldsymbol{r}) = \psi^\dagger(\boldsymbol{r})\boldsymbol{\sigma}\psi(\boldsymbol{r}), \tag{12}$$

and μ_B the Bohr magneton. For our quasi-1D geometry, we can rewrite the components of $\boldsymbol{m}$ in terms of the quasiparticle amplitudes:

$$\begin{aligned} m_x(x) = &-\mu_B\sum_n\{[u_{n\uparrow}^*(x)u_{n\downarrow}(x) + u_{n\downarrow}^*(x)u_{n\uparrow}(x)]f_n \\ &- [v_{n\uparrow}(x)v_{n\downarrow}^*(x) + v_{n\downarrow}(x)v_{n\uparrow}^*(x)](1-f_n)\}, \end{aligned} \tag{13}$$

$$\begin{aligned} m_y(x) = &-i\mu_B\sum_n\{[u_{n\uparrow}(x)u_{n\downarrow}^*(x) - u_{n\downarrow}(x)u_{n\uparrow}^*(x)]f_n \\ &+ [v_{n\uparrow}(x)v_{n\downarrow}^*(x) - v_{n\downarrow}(x)v_{n\uparrow}^*(x)](1-f_n)\}, \end{aligned} \tag{14}$$

$$\begin{aligned} m_z(x) = &-\mu_B\sum_n\{[|u_{n\uparrow}(x)|^2 - |u_{n\downarrow}(x)|^2]f_n \\ &+ [|v_{n\uparrow}(x)|^2 - |v_{n\downarrow}(x)|^2](1-f_n)\}. \end{aligned} \tag{15}$$

We now turn to the appropriate expressions for the currents. As stressed in Sec. I, one needs to carefully establish proper conservation laws when discussing the transport properties of the system [56]. We first discuss the charge supercurrent.

In our geometry, the charge current has only one component J_x, which depends on the x coordinate. In the absence of an external magnetic field, the total charge current $J_x(x) \equiv J_{x\uparrow}(x) + J_{x\downarrow}(x)$ is found from the standard quantum mechanical expression $J_x = (e/m)\langle\psi^\dagger p_x \psi\rangle$. This leads to the result

$$J_{x\sigma}(x) = \frac{e}{2m}\left\langle -i\psi_\sigma^\dagger \frac{\partial}{\partial x}\psi_\sigma + i\left(\frac{\partial}{\partial x}\psi_\sigma^\dagger\right)\psi_\sigma \right\rangle. \tag{16}$$

This expression for the current ensures, together with the self-consistency condition, that charge conservation is satisfied, that is, $dJ_x/dx = 0$ in the steady state [38,46,57]. It is of course convenient numerically to rewrite the expression for the current in terms of the calculated quasiparticle amplitudes and energies. After inserting the Bogoliubov transformations in Eq. (2), we can write the total charge current, as given by Eq. (16), summed over spins as

$$J_x(x) = \frac{2e}{m}\sum_{n,\sigma}\mathrm{Im}\left[u_{n\sigma}\frac{\partial u_{n\sigma}^*}{\partial x}f_n + v_{n\sigma}\frac{\partial v_{n\sigma}^*}{\partial x}(1-f_n)\right]. \tag{17}$$

One can verify once again the conservation law by taking the divergence of the current in Eq. (17) and using the BdG equations (4) to find [38,46]

$$\frac{\partial J_x(x)}{\partial x} = 2e\,\mathrm{Im}\left\{\Delta(x)\sum_n [u_{n\uparrow}^* v_{n\downarrow} + u_{n\downarrow}^* v_{n\uparrow}]\tanh\left(\frac{\epsilon_n}{2T}\right)\right\}. \tag{18}$$

When the self-consistency condition is satisfied, the right-hand side vanishes, and charge is properly conserved. If the self-consistency condition is not strictly satisfied, the terms on the right side act effectively as sources or sinks of current [38,46,57]. We will consider large-S contacts with the amplitude and phase of the order parameter determined self-consistently except near the sample edges (see Appendix A) where sources and sinks of charge exist via the implicit external electrodes. This gives the necessary charge conservation condition in the region of interest. We emphasize here that with self-consistent solutions, we are able to correctly determine the effect of triplet correlations on both the charge and spin transport.

The extension of the above considerations to spin transport is relatively straightforward [38,49]. As in the case of the charge density, the Heisenberg picture is utilized to determine the time evolution of the spin density $\boldsymbol{\eta}(\boldsymbol{r},t)$,

$$\frac{\partial}{\partial t}\langle\boldsymbol{\eta}(\boldsymbol{r},t)\rangle = i\langle[\mathcal{H},\boldsymbol{\eta}(\boldsymbol{r},t)]\rangle, \tag{19}$$

where $\boldsymbol{\eta}$ is given in Eq. (12). The associated continuity equation now reads as

$$\frac{\partial}{\partial t}\langle\boldsymbol{\eta}(\boldsymbol{r},t)\rangle + \frac{\partial \boldsymbol{S}}{\partial x} = \boldsymbol{\tau} + \mathcal{J}_S, \tag{20}$$

where $\boldsymbol{S}$ is the spin current which in our geometry is a vector (in general it is a tensor). The spin-transfer torque $\boldsymbol{\tau}$ is given by

$$\boldsymbol{\tau} = -i\langle\psi^\dagger(\boldsymbol{r})[\boldsymbol{h}\cdot\boldsymbol{\sigma},\boldsymbol{\sigma}]\psi(\boldsymbol{r})\rangle = 2\langle\psi^\dagger(\boldsymbol{r})[\boldsymbol{\sigma}\times\boldsymbol{h}]\psi(\boldsymbol{r})\rangle. \tag{21}$$

The $\mathcal{J}_S$ term has components

$$\mathcal{J}_{Sx} = 2\,\mathrm{Im}\{\Delta\langle\psi_\downarrow^\dagger(\boldsymbol{r})\psi_\uparrow^\dagger(\boldsymbol{r}) - \psi_\uparrow^\dagger(\boldsymbol{r})\psi_\downarrow^\dagger(\boldsymbol{r})\rangle\}, \tag{22}$$

$$\mathcal{J}_{Sy} = 2\,\mathrm{Re}\{\Delta\langle\psi_\downarrow^\dagger(\boldsymbol{r})\psi_\downarrow^\dagger(\boldsymbol{r}) + \psi_\uparrow^\dagger(\boldsymbol{r})\psi_\uparrow^\dagger(\boldsymbol{r})\rangle\}. \tag{23}$$

For the s-wave superconductors considered in this paper, we have $\mathcal{J}_S = 0$ by virtue of the Pauli principle since only equal time correlations are involved. Thus, in the absence of spin-transfer torque, we have $\partial\boldsymbol{\eta}/\partial t + \partial\boldsymbol{S}/\partial x = 0$. However, in general [38] spin-transfer torque is present and, in the steady state, the derivatives of $\boldsymbol{S}$ with respect to x do not vanish.

The expression for the spin current $\boldsymbol{S}$ is found from taking the commutator in Eq. (19) and using Eq. (1):

$$\boldsymbol{S} = -\frac{i}{2m}\left\langle\psi^\dagger(\boldsymbol{r})\boldsymbol{\sigma}\frac{\partial\psi(\boldsymbol{r})}{\partial x} - \frac{\partial\psi^\dagger(\boldsymbol{r})}{\partial x}\boldsymbol{\sigma}\psi(\boldsymbol{r})\right\rangle, \tag{24}$$

where we recall that the vector $\boldsymbol{S}$ represents spin current flowing along the x direction for our quasi-one-dimensional systems. We can now expand each spin component of the spin current in terms of the quasiparticle amplitudes to obtain

$$\boldsymbol{S}_x = -\frac{i}{2m}\sum_n\left\{f_n\left[u_{n\uparrow}^*\frac{\partial u_{n\downarrow}}{\partial x} + u_{n\downarrow}^*\frac{\partial u_{n\uparrow}}{\partial x} - u_{n\downarrow}\frac{\partial u_{n\uparrow}^*}{\partial x} - u_{n\uparrow}\frac{\partial u_{n\downarrow}^*}{\partial x}\right] - (1-f_n)\left[v_{n\uparrow}\frac{\partial v_{n\downarrow}^*}{\partial x} + v_{n\downarrow}\frac{\partial v_{n\uparrow}^*}{\partial x} - v_{n\uparrow}^*\frac{\partial v_{n\downarrow}}{\partial x} - v_{n\downarrow}^*\frac{\partial v_{n\uparrow}}{\partial x}\right]\right\}, \tag{25}$$

$$\boldsymbol{S}_y = -\frac{1}{2m}\sum_n\left\{f_n\left[u_{n\uparrow}^*\frac{\partial u_{n\downarrow}}{\partial x} - u_{n\downarrow}^*\frac{\partial u_{n\uparrow}}{\partial x} - u_{n\downarrow}\frac{\partial u_{n\uparrow}^*}{\partial x} + u_{n\uparrow}\frac{\partial u_{n\downarrow}^*}{\partial x}\right] - (1-f_n)\left[v_{n\uparrow}\frac{\partial v_{n\downarrow}^*}{\partial x} - v_{n\downarrow}\frac{\partial v_{n\uparrow}^*}{\partial x} + v_{n\uparrow}^*\frac{\partial v_{n\downarrow}}{\partial x} - v_{n\downarrow}^*\frac{\partial v_{n\uparrow}}{\partial x}\right]\right\}, \tag{26}$$

$$\boldsymbol{S}_z = -\frac{i}{2m}\sum_n\left\{f_n\left[u_{n\uparrow}^*\frac{\partial u_{n\uparrow}}{\partial x} - u_{n\uparrow}\frac{\partial u_{n\uparrow}^*}{\partial x} - u_{n\downarrow}^*\frac{\partial u_{n\downarrow}}{\partial x} + u_{n\downarrow}\frac{\partial u_{n\downarrow}^*}{\partial x}\right] - (1-f_n)\left[-v_{n\uparrow}\frac{\partial v_{n\uparrow}^*}{\partial x} + v_{n\uparrow}^*\frac{\partial v_{n\uparrow}}{\partial x} + v_{n\downarrow}\frac{\partial v_{n\downarrow}^*}{\partial x} - v_{n\downarrow}^*\frac{\partial v_{n\downarrow}}{\partial x}\right]\right\}. \tag{27}$$

In the case of F layers with uniform magnetization, there is no net spin current. The introduction of an inhomogeneous magnetization texture, however, results in a net spin current imbalance that is finite [38] even in the absence of a Josephson current. This will be discussed in greater detail in the following.

To compute the spin-transfer torque, it is useful to express it in terms of the quasiparticle amplitudes. A convenient

approach involves directly taking the expectation values of Eq. (21):

$$\boldsymbol{\tau} = 2\langle\psi^{\dagger}(\boldsymbol{r})\boldsymbol{\sigma}\psi(\boldsymbol{r})\rangle \times \boldsymbol{h} = -\frac{2}{\mu_B}\boldsymbol{m} \times \boldsymbol{h}, \tag{28}$$

where we have used Eq. (11). The magnetization components are given in Eqs. (13)–(15). Since the exchange field $\boldsymbol{h}$ is prescribed, it is the self-consistently calculated magnetization that determines the torque acting on the ferromagnet layers. Equivalently, one can use the continuity equation in the steady state to determine the torque transfer by evaluating the derivative of the spin current as a function of position:

$$\boldsymbol{\tau}_i = \frac{\partial \boldsymbol{S}_i}{\partial x}. \tag{29}$$

It is, however, safer to evaluate both sides of Eq. (29) independently and use this equation as a consistency check. We have performed extensive numerical checks using this procedure. In most of the results presented we have calculated the torques using Eq. (28), thus avoiding the numerical derivatives that arise when using the right side of Eq. (29). Additional physical insight can be gained by integrating Eq. (29) over a particular region, e.g., F_1:

$$\boldsymbol{S}_x(b) - \boldsymbol{S}_x(a) = \int_{\mathrm{F_1}} dx\, \tau_x = \tau_{x,\mathrm{tot}}, \tag{30}$$

which means that the change in spin current through $\mathrm{F_1}$ (from $x = a$ to b) is equivalent to the net torque acting within those boundaries.

III. RESULTS

The results of our systematic investigations are presented in terms of convenient dimensionless quantities. Our choices are as follows: all length scales, including the position $X \equiv k_F x$, and widths $D_{Fi} \equiv k_F d_{Fi}$ $(i = 1,2,3)$ are normalized by the Fermi wave vector k_F. For the superconducting correlation length ξ we choose the value $k_F\xi = 100$, and the computational region occupied by the S electrodes corresponds to a width of 8ξ (see Appendix B for numerical details). All temperatures are measured in units of T_{c0}, the transition temperature of bulk S material, and we consider the low-temperature regime $T/T_{c0} = 0.01$. Energy scales are normalized by the Fermi energy ε_F, including the Stoner field interaction $\boldsymbol{h}$ and the energy cutoff ω_D, used in the self-consistency condition Eq. (7). The latter is set at 0.04: results are often independent of this cutoff choice. As mentioned above, the strength of the magnetic exchange fields h is taken to be the same in both magnets: we set its dimensionless value to a representative $h = 0.1$. We vary the orientation angles of the magnetic exchange field in each of the F regions, depending on the quantity being studied. The magnetization is normalized by $\mu_B n_e$, where n_e is the electron density $n_e = k_F^3/(3\pi^2)$. The normalization τ_0 for the torque follows from the normalizations for h and $\boldsymbol{m}$ and Eq. (28). When presenting results for the currents, we normalize the charge current densities J_x by J_0, where $J_0 \equiv en_e v_F$, and $v_F = k_F/m$ is the Fermi velocity. All three components of the spin current $\boldsymbol{S}$ are normalized similarly, by the quantity S_0, where S_0 involves the normalization of $\boldsymbol{m}$ and a factor of $n_e v_F$. The interface scattering $U(x)$ is represented by delta functions of strength H at all the interfaces. The corresponding dimensionless parameter is $H_B \equiv H/v_F$. The self-consistency of the pair potential that characterizes an accurate representation of the Cooper pair correlations throughout the system is associated with the proximity effects and depends to varying degrees on the parameters outlined above. In some cases, the dependence is rather obvious: for instance, large H_B results in weaker proximity effects. In other cases, it is more intricate and will be analyzed more carefully.

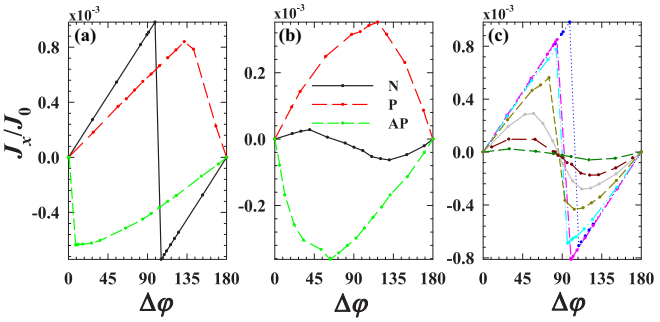

FIG. 2. (Color online) Normalized (see text) Josephson current versus phase difference $\Delta\varphi$ for a SF_1F_2S structure with $D_{F_1} = 10$, $D_{F_2} = 100$, and $h = 0.1$. For panels (a) and (b), the legend in (b) labels the relative in-plane magnetization orientations: parallel (P), antiparallel (AP), or normal (N). Two interface scattering strengths are considered: (a) $H_B = 0$ and (b) $H_B = 1$. In panel (c), the magnetization orientations are fixed in the normal configuration ($\phi_1 = 0$, $\phi_2 = 90^\circ$), and the interface scattering is varied as $H_B = 0,0.2,0.5,0.6,0.7,0.8,1$ (in descending order of peaks).

A. Current-phase relations

We begin by showing our results for the self-consistent current-phase relations in a simple double-layer ferromagnet Josephson junction. At the interfaces between the F and S regions, quasiparticles undergo Andreev and conventional reflections [58–61]. The superposition of these waves in the F regions results in subgap bound states that contribute, together with the continuum states, to the total current flow. In Fig. 2, we show the supercurrent as a function of phase difference (current-phase relation CPR) for two ferromagnets of unequal width: $D_{F_1} = 10$ and $D_{F_2} = 100$. This asymmetric choice of widths helps ensure [12,19] that equal-spin triplet correlations are generated in the system. The angular parameters in this figure are fixed at $\theta_1 = 90^\circ$ and $\theta_2 = 90^\circ$, corresponding to in-plane magnetization orientations. The F_1 layer has its magnetization aligned in the z direction ($\phi_1 = 0^\circ$). The first two panels (a) and (b) display three different relative in-plane magnetization configurations in the F_2 layers: parallel (P) ($\phi_2 = 0^\circ$), antiparallel (AP) ($\phi_2 = 180^\circ$), and normal (N) [62] ($\phi_2 = 90^\circ$). Two different strengths of the interface scattering parameter are considered. In (a) there is no interface scattering ($H_B = 0$), while in (b), a rather high rate of scattering is present, with $H_B = 1$. The CPR for the collinear configurations (P or AP) possesses the conventional 2π periodicity, and the supercurrent flows oppositely for the two alignments. When the relative magnetizations are orthogonal to each another, the CPR becomes π periodic as revealed

by the sawtoothlike pattern in (a) or the more sinusoidal behavior in (b), both of which change sign at $\Delta\varphi \approx 90^\circ$. This is a consequence of the emergence of equal-spin triplet correlations [17,32,42–45] that are absent when the exchange fields in the ferromagnets point along the same direction. When strong interface scattering is present, Fig. 2(b) shows that the π-periodic CPR (N case) is substantially diminished, relative to the P or AP cases. This is because the proximity effect is weakened, with a resulting reduction of the associated equal-spin triplet correlations. To further examine the effects that interface scattering has on this π-periodic supercurrent, we consider in Fig. 2(c) the same SF_1F_2S junction with varying degrees of scattering strengths H_B and with the relative in-plane magnetizations fixed and orthogonal to each another ($\phi_2 = 90^\circ$). Increasing H_B clearly leads to a crossover in the CPR from a sawtooth to sinusoidal form and to a marked reduction of the supercurrent flow. As this occurs, the phase difference $\Delta\varphi$ yielding the critical current density also declines.

We next consider, in Fig. 3, the effect on the CPR of changing D_{F_1} and D_{F_2} in a SF_1F_2S structure. Figures 3(a)–3(c) label the various widths D_{F_1} considered. We keep $D_F \equiv$

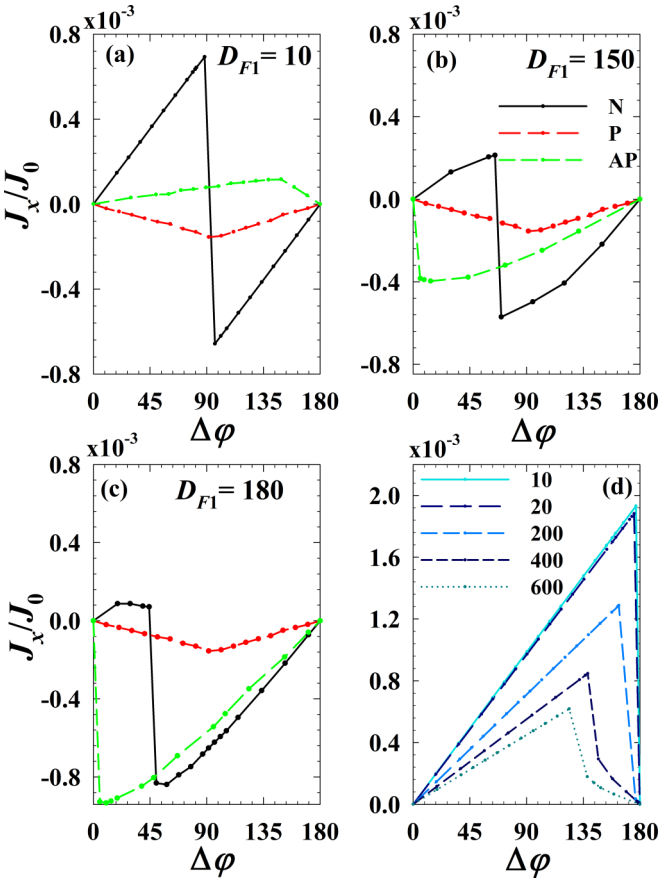

FIG. 3. (Color online) Normalized Josephson current versus phase difference $\Delta\varphi$ for a SF_1F_2S structure with no interface scattering, $H_B = 0$. In panels (a)–(c), various widths of the F regions are considered, each panel labeled by the width D_{F_1} of the ferromagnet layer F_1, with the constraint that $D_{F_1} + D_{F_2} = 390$. The legend in (b) labels the relative magnetization orientation (see Fig. 2). In (d) the magnetization configuration is N, $D_{F_1} = D_{F_2}$, and their individual widths are given in the legend.

$D_{F_1} + D_{F_2}$ fixed to a representative value of $D_F = 390$. In Figs. 3(a)–3(c), we consider the same three magnetization orientations as in Fig. 2. One sees that, in the N configuration, the structure with the greatest geometric asymmetry, as given by the ratio D_{F_1}/D_{F_2}, tends to have a more pronounced superharmonic CPR relative to the P and AP collinear configurations. Upon increasing D_{F_1}, the jagged sawtooth peaks at $D_{F_1} = 10$ become smoothed and the π-periodic CPR is reduced substantially. The observed reversal of current direction for a given magnetic configuration when changing the F widths is a direct consequence of the damped oscillatory behavior of the singlet and triplet correlations, as will be discussed following (see also Fig. 8). By comparing Fig. 3(a) with Fig. 2(a) and noting that the only difference between them is the thickness of the second magnet, one finds that the magnitude of the supercurrent for the N case with thicker F_2 does not drop significantly, as it does in the P and AP configurations. Such behavior is a signature of the long-range nature of the equal-spin triplet correlations. To show further the effects of increased width on the supercurrent, we consider in Fig. 3(d) the symmetric geometry configuration for several equal F layer widths D_F. As shown in the legend, a broad range of D_F is considered. It is clear from the figure that the equal-spin triplet correlations responsible for the previously observed superharmonic CPRs are strongly impacted, and only a 2π-periodic supercurrent arises. By increasing the ferromagnet widths, the rate at which the current changes with $\Delta\varphi$ tends to decline for wider junctions, and the "critical" $\Delta\varphi$ where the current is suddenly reduced becomes smaller. In this panel, the ferromagnetic region is no longer constrained to have the same total width, hence, increasing D_F reduces the overall current flow.

We now consider a trilayer junction, where a nonmagnetic normal-metal "spacer" separates the two ferromagnets. Such spacers are convenient experimentally when it is wished [19] to rotate the magnetization in one magnet only. We focus on the case where the CPRs have important additional harmonics: we keep the in-plane mutual magnetizations orthogonal (with $\phi_2 = 90^\circ$ and $\theta_2 = 90^\circ$). In Figs. 4(a) and 4(b), the ferromagnet widths are $D_{F_1} = 10$ and $D_{F_3} = 100$, while the width of the normal metal spacer D_N varies from 0 to 500 (corresponding to $0 \leqslant d_N/\xi \leqslant 5$) as indicated in the legend. The interface scattering parameter is $H_B = 0.5$ for Fig. 4(a) and $H_B = 0.8$ in Fig. 4(b). In either case, increasing D_N leads to an overall reduction in the supercurrent flow. For large interface scattering, the CPR becomes less sensitive to D_N. A wider junction, with ferromagnet widths $D_{F_1} = 10$ and $D_{F_3} = 380$, is shown in (c), with $H_B = 0$. The details of the usual sawtooth CPR reveal that the supercurrent flow can be quite sensitive to the spacer width, as it abruptly reverses direction at considerably different phase differences, for incremental changes in D_N. In this panel, results for an additional small value of the spacer thickness $D_N = 5$ are also shown. Since the π-periodic CPR is closely related to the generation of the equal-spin triplet correlation, one can infer from Fig. 4 that the introduction of an additional nonmagnet metallic layer can quantitatively changes the transport properties. In Sec. III C, we will discuss connections between the results in this figure and those for the induced triplet correlations to be shown in Figs. 9 and 10.

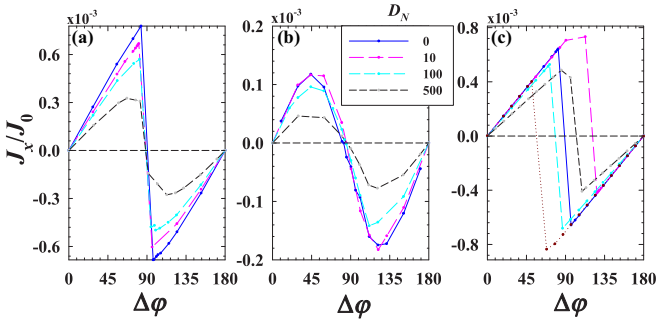

FIG. 4. (Color online) Normalized Josephson current versus $\Delta\varphi$ for a SF_1NF_3S structure. The legend labels the N spacer widths D_N. The relative in-plane magnetization angle between the two F layers is 90°. For panels (a) and (b), the layers F_1 and F_3 have widths $D_{F_1} = 10$ and $D_{F_3} = 100$. In panel (a) $H_B = 0.5$, in panel (b) $H_B = 0.8$, and in panel (c) $H_B = 0$, with ferromagnet widths $D_{F_1} = 10$ and $D_{F_3} = 380$. In panel (c) the additional dotted curve corresponds to $D_N = 5$, illustrating the sensitivity of the current phase relation to D_N.

To examine the effects of increased magnetic inhomogeneity, we show in Fig. 5 results for a pentalayer $SF_1F_2F_3S$ junction. This structure is complementary to that studied in Fig. 3, the main difference being an additional ferromagnet layer F_2 with an out-of-plane magnetic exchange field oriented in the x direction (corresponding to $\theta_2 = 0°$ in Fig. 1). The relative magnetic orientations are labeled in the legend by the directions of the axes along with the magnetizations are aligned in each F layer. For example, $z/x/y$ denotes a sample in which F_1 and F_3 are normal to each other (the configuration labeled N in the previous figures) with an additional out-of plane magnetization in F_2. The width of the F_2 layer is identical to that of the F_1 layer: $D_{F_1} = D_{F_2} = 10$ in Fig. 5(a) and $D_{F_1} = D_{F_2} = 20$ in Fig. 5(b). The thicker ferromagnet F_3 has width $D_{F_3} = 380$. The π-periodic CPR that arises in double magnet SF_1F_2S junctions with orthogonal in-plane magnetizations remains relatively unchanged by the addition of the additional out-of-plane intermediate ferromagnet. However, it was shown in Figs. 3(a)–3(c) that the collinear P or AP magnetic states still

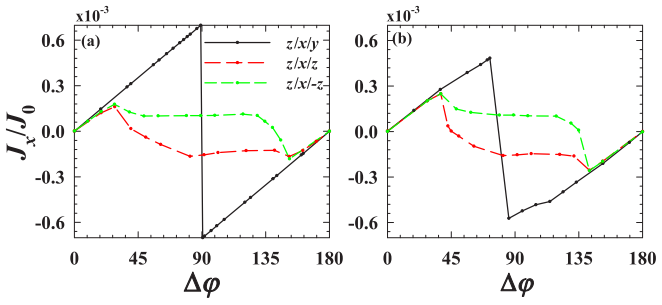

FIG. 5. (Color online) Normalized Josephson current versus $\Delta\varphi$ for a $SF_1F_2F_3S$ structure. The legend labels the three relative magnetization directions between the F layers. They correspond in order to the configurations labeled N, P, and AP in the previous figures for F_1 and F_3, while the intermediate layer F_2 has out-of-plane magnetization. The ferromagnetic layer F_3 has a fixed width corresponding to $D_{F_3} = 380$. The adjacent F layers have widths [panel (a)] $D_{F_1} = D_{F_2} = 10$ and [panel (b)] $D_{F_1} = D_{F_2} = 20$.

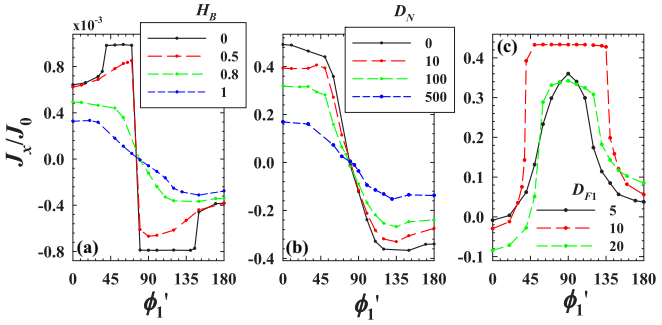

FIG. 6. (Color online) Normalized Josephson current versus the in-plane relative magnetization angle $\phi_1' \equiv \phi_1 + 90°$ (see text), for a SF_1F_2S junction (a), and for a SF_1NF_3S junction with $H_B = 0.8$ (b). The legends show the geometric and material parameters that are varied. In (a) $\Delta\varphi = 100°$, $D_{F_1} = 10$, and $D_{F_2} = 100$. In (b) $\Delta\varphi = 100°$, $D_{F_1} = 10$, and $D_{F_3} = 100$. In (c) an SF_1F_2S junction is considered with $H_B = 0$ and $\Delta\varphi = 60°$. The outer ferromagnet layer has $D_{F_2} = 380$, while three different D_{F_1} values are considered (see legend).

with 2π periodicities behaved in an approximately piecewise linear fashion and that the current maintained its direction when varying $\Delta\varphi$. Now, on the other hand, the insertion of an additional F layer between the collinear ferromagnets makes it possible for equal-spin triplet correlations to be generated and the supercurrent becomes drastically modified. For phase differences in the vicinity of 0 or π, Figs. 5(a) and 5(b) show that the current is approximately linear in the phase difference, but there is a broad intermediate range of $\Delta\varphi$, where the supercurrent flow is relatively uniform. Moreover, for either the P or AP configuration, varying the phase can result in the Josephson current switching direction. These trends are the same for each of the cases presented in Figs. 5(a) or 5(b).

B. Magnetic orientation and CPR

Having discussed the current phase relations for a few different ferromagnetic Josephson junction configurations, we now will study in more detail the effect of varying magnetization orientations on the CPR. We will set the macroscopic phase difference to a prescribed value and study the supercurrent response within the junctions for a range of relative magnetization orientations.

We begin with a basic SF_1F_2S Josephson junction whose phase difference is set at $\Delta\varphi = 100°$. We consider in Fig. 6(a) the normalized supercurrent density as a function of the in-plane magnetization angle ϕ_1' ($\theta_1 = 90°$), where $\phi_1' \equiv \phi_1 + 90°$, with ϕ_1 being the angle shown in Fig. 1. The P and AP states correspond to $\phi_1' = 0°$ and $\phi_1' = 180°$, respectively (since the magnetization in F_2 is fixed along y). Four interface scattering strengths are considered in Fig. 6(a), as indicated in its legend. In all cases, by tuning the relative alignment angles, supercurrent switching occurs when the mutual magnetization orientations are approximately orthogonal. As expected, the supercurrent flow is greatest for transparent interfaces ($H_B = 0$), and decreases with increasing H_B, as the sensitivity to ϕ_1' becomes weaker. The maximum current flow occurs at different ϕ_1' values, depending on the interface scattering strength. In Fig. 6(b), an additional N layer, of variable

width as indicated, is inserted between the two ferromagnets and the interface scattering parameter is set to $H_B = 0.8$. The solid $D_N = 0$ curve corresponds to the $H_B = 0.8$ curve in Fig. 6(a). The figure shows that increasing the N layer thickness tends to generally dampen the current through the junction. The current flow peaks when the two ferromagnets are aligned (P configuration) and it vanishes altogether near the N arrangement, before reversing direction as the the AP state is approached. In Fig. 6(c), we investigate the supercurrent flow in a wide SF_1F_2S junction, with $D_{F_2} = 500$ and three F_1 widths (see legend). The phase difference is set at $\Delta\varphi = 60^\circ$. For this geometry, we see that the current has some features that contrast with the previous cases involving thinner F layers. For instance, when tuning ϕ_1', now the weakest current flow occurs in the P state, and the maximum occurs in the orthogonal configuration. For all F widths considered, the current undergoes rapid changes in the vicinity of the middle value between N and P or N and AP configurations, with the $D_{F_1} = 10$ case changing the most, and then remains nearly constant at angles near the P and AP configurations. Since $\Delta\phi = 60^\circ$ is near where the maximum currents occur in π-periodic Josephson junctions, it is evident that the results in Fig. 6(c) are a direct consequence of the induced equal-spin triplet correlations. We will see in Sec. III C that this correlates with the triplet generation behavior.

We next study the magnetization orientation role in the supercurrent for more complicated $SF_1F_2F_3S$ junctions. We consider a scenario where the F_1 and F_3 layers have magnetizations pinned along the z and y directions, respectively (a relative N configuration), while the magnetization in the central F layer rotates on the $x - z$ plane ($\phi_2 = 0$) from along the x axis to the z axis. In Fig. 7(a), we show the normalized current density as a function of θ_2 for several F_3 layer widths D_{F_3}. We set $D_{F_1} = D_{F_2} = 10$, and consider values of D_{F_3} that lead to both symmetric and asymmetric structures. In each case, $\Delta\varphi = 100^\circ$, and interface scattering is present with $H_B = 0.8$, except for the widest junction with $D_{F_3} = 380$

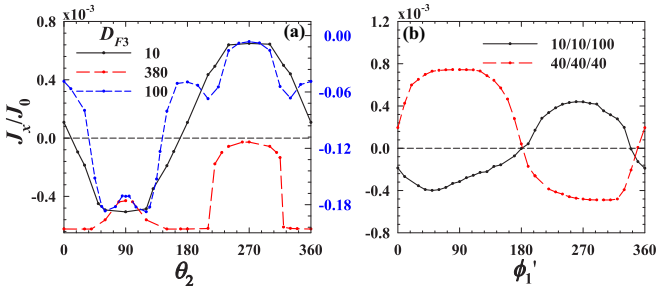

FIG. 7. (Color online) Normalized Josephson current for a $SF_1F_2F_3$S junction versus (a) the out-of-plane angle θ_2 (see Fig. 1) and (b) the in-plane angle ϕ_1'. A set phase difference $\Delta\varphi = 100^\circ$ is assumed for all cases. In (a), F_1 and F_2 have widths $D_{F_1} = D_{F_2} = 10$, and the legend lists the three F_3 widths considered. The exchange field points along the y direction in F_3 and the z direction in F_1. The right vertical axis is for the $D_{F_3} = 100$ case only. For the $D_{F_3} = 380$ case, there is no interface scattering ($H_B = 0$), while the remaining D_{F_3} cases have $H_B = 0.8$. In (b) $\theta_1 = 90^\circ$, and $\boldsymbol{h}$ is directed along y in F_2, and along z in F_3. The legend indicates the F layer widths of the two trilayer ferromagnet structures considered: they have the same total width. Interface scattering in both cases is $H_B = 0.8$.

where $H_B = 0$. In the case $D_{F_1} = D_{F_2} = D_{F_3} = 10$, the current flow is approximately antisymmetric around $\theta_2 = 180^\circ$. The current flow is suppressed for the asymmetric $D_{F_3} = 100$ situation by decoherence effects arising from the larger width. While J_x for the SF_1F_2S junctions in Fig. 6 was π periodic in ϕ_1', variations in θ_2 for trilayer ferromagnetic junctions are in general 2π periodic, as seen in the figure. The asymmetric case also exhibits a more intricate structure as the magnetization angle is swept. For the narrower junction $D_{F_3} = 10$, the orientations in which the current switches direction are near $\theta_2 = 0^\circ$ and 180°. When $D_{F_3} = 100$, the current never changes direction. The rotating out-of-plane exchange field of F_2 does affect the strength of current with 2π periodicity. For the highly asymmetric $D_{F_3} = 380$ case, the current again maintains its flow direction over the full range of θ_2. It is also approximately constant except for orientations when the exchange field in F_2 points along z: $\theta_2 = 90^\circ$ or 270°. For orientations near $\theta_2 = 270^\circ$, the current is strongly suppressed.

In Fig. 7(b), the in-plane magnetization in the first ferromagnetic layer is now varied, while the other two are kept fixed: for F_2 along y, and for F_3 along z, an N configuration. Two types of structures are considered, with the total width of the three ferromagnetic regions being constant. In the first case, $D_{F_1} = D_{F_2} = 10$, and $D_{F_3} = 100$, while in the second one, $D_{F_1} = D_{F_2} = D_{F_3} = 40$. Both cases exhibit similar behavior as a function of ϕ_1'. The current vanishes when F_1 is antiparallel to F_2 and is highest when the magnetization lies nearly in between the those of F_2 and F_3. Thus, the charge supercurrent which flows oppositely in the two structures can be effectively switched on or off by manipulating the in-plane magnetization angle of the first ferromagnet.

It is known that in F/S heterostructures, including bilayers [29] and Josephson junctions, variations in the magnetic exchange field and ferromagnet thickness induce damped oscillations in the spatial behavior of the Cooper pair amplitudes, resulting in modulation of physical quantities as a function of either h or D_F. The damped oscillations in the clean limit have a wavelength that goes as the inverse of the exchange field. To investigate this phenomenon in an SF_1F_2S junction, we show in Fig. 8 the supercurrent that flows through the junction as a function of the F_1 width D_{F_1}. For the adjacent F_2 layer, the width is $D_{F_2} = 100$, and with interface scattering strength $H_B = 0.8$. Two exchange fields are considered: $h = 0.04$ and 0.1. The period of oscillations in each case is seen to be approximately $2\pi k_F\xi_F$, where $k_F\xi_F \equiv \varepsilon_F/h = 25$ and 10, respectively. The current for both cases is maximal when the two F regions are equal, and then slowly dampens out with increasing D_{F_1}. This decay length is inversely proportional to the magnitude of the exchange field. Moreover, the charge current in each case periodically changes sign. Since the oscillations in the current as a function of D_{F_1} increase with larger exchange fields, the current direction can be very sensitive to fabrication tolerances for strong magnets.

C. Induced triplet pairing

We now discuss the induced triplet pairing correlations in ferromagnetic Josephson junctions. The presence of multiple misaligned ferromagnets yields both the $m = 0$ [Eq. (9)] and the $m = \pm 1$ [Eq. (10)] triplet pair amplitudes as permitted by conservation laws and the Pauli principle. To gain an

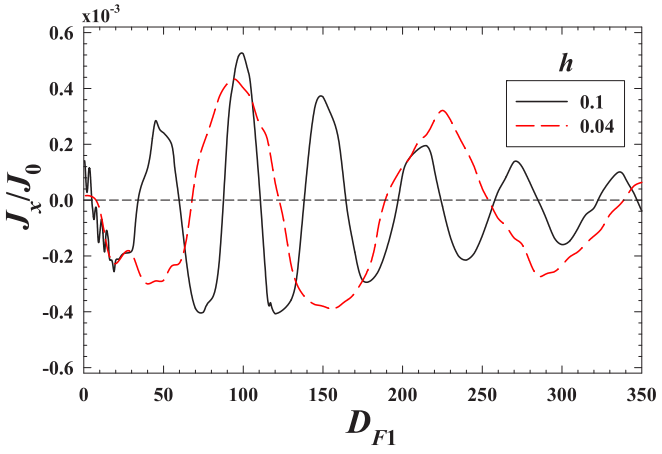

FIG. 8. (Color online) Normalized Josephson current for a SF_1F_2S structure as a function of F layer width D_{F_1}. The other ferromagnet's width is fixed at $D_{F_2} = 100$. The exchange field is along z in F_1 and along y in F_2. The legend indicates two normalized h values: the dashed curve corresponds to $h = 0.04$, while the solid curve is for $h = 0.1$. The interface scattering parameter is set to $H_B = 0.8$, and a phase difference of $\Delta\varphi = 100^\circ$ is maintained across the S electrodes.

overall view of the opposite-spin triplet amplitudes f_0 and the equal-spin amplitudes f_1, we illustrate in Fig. 9 the spatial behavior of these correlations in the N and F regions of an SF_1NF_3S junction. We focus on the real parts of these complex quantities, keeping in mind that the imaginary components obey similar trends. The vast majority of previous studies of triplet correlations in these double-magnet structures are in the diffusive regime and do not include [2,13,27,39] the

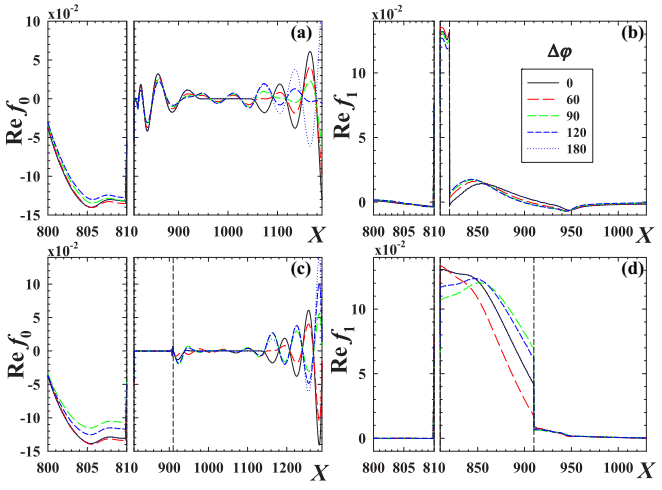

FIG. 9. (Color online) Normalized triplet correlations in an SF_1NF_3S Josephson junction as a function of position. The F layers have widths $D_{F_1} = 10$ and $D_{F_3} = 380$, and $H_B = 0$, corresponding to the parameters used in Fig. 4(c). The top set of panels relate to structures with a normal-metal spacer N of width $D_N = 10$, while the bottom set represent a larger N layer with $D_N = 100$. The dashed vertical lines represent the interface between the N and F_2 regions. Various phase differences $\Delta\varphi$ are considered (see legend). The magnetization in F_1 is along z, while it is along y in F_2.

normal-metal insert actually present in most experiments. In the ballistic regime, double-magnet structures were studied only in the quasiclassical limit [12,63]. The scope of their results is thus limited to weak magnets. By fully taking into account the microscopic proximity effects between all of the interacting layers, we demonstrate that the interference effects taking place over the Fermi length scale combined with the self-consistency of the pair potential create the interesting local spatial behavior.

The geometrical parameters in this figure are $D_{F_1} = 10$, $D_{F_3} = 380$, and $D_N = 10$ (top panels) or $D_N = 100$ (bottom panels). Thus, in all panels the region $800 < X < 810$ is occupied by F_1 while F_3 occupies the region $820 < X < 1200$ in the top panels and $910 < X < 1290$ in the bottom panels Figs. 9(c) and 9(d), where the vertical dotted line denotes the N spacer boundary. Hence, different horizontal scales are used in each case. The scattering parameter is set to $H_B = 0$, and each curve corresponds to a different phase difference $\Delta\varphi$ as indicated by the legend. The exchange fields are in-plane and normal to each other. Within the F_1 region, Figs. 9(a) and 9(c) reveal that the magnitude of the f_0 pair correlations are approximately of the same magnitude, decreasing in the vicinity of the S/F interface located at $X = 800$. The system with the wider normal-metal layer $D_N = 100$ is slightly more sensitive to phase variations. Within the ferromagnet F_3, Figs. 9(a) and 9(c) show the oscillatory nature of f_0, which behaves similarly to the singlet pair amplitude, the periodicity arising from the difference in spin-up and spin-down wave vectors. For the chosen exchange field, the oscillations are limited in F_1 due to the confined width. Turning now to the equal-spin triplet correlations f_1, Figs. 9(b) and 9(d) display behavior which contrasts with the f_0 results. In particular, within the narrow F_1 region, the f_1 triplets are negligibly small, and the f_0 correlations clearly dominate. In the N region, the f_0 correlations nearly vanish, while the equal-spin triplets peak near the F_1/N interface (at $X = 810$), before dropping within the normal metal [see Fig. 9(d)]. Finally, within F_3, the triplets f_1 assume a slow, long-range variation compared to the damped oscillatory behavior of the f_0 curves. Thus, we have shown a large enhancement of triplet correlations consisting of equal-spin pairs that reside in the nonmagnetic normal metal regardless of whether the width of N is relatively thin or thick. For the thick N case shown in Fig. 4(c), the maximum in the CPR occurs at $\Delta\varphi = 90$. Remarkably, the corresponding f_0 is weakest in F_1 but f_1 is very uniformly distributed in N.

In addition to investigating the relevant spatial behavior of the triplet amplitudes, it is instructive to also examine the spatially averaged triplet and singlet correlations as functions of the relevant system parameters. For example, by tuning the relative magnetization angle (varying ϕ_1' at fixed $\phi_2 = 90^\circ$), important overall features can be revealed. Figures 10(a)–10(c) show the ϕ_1' dependence of the magnitudes of the triplet and singlet amplitudes averaged over the F_3 region for the SF_1NF_3S structure studied initially in Fig. 6(b). Four representative N layer widths are considered as indicated in the legend. The proximity effects and hence coupling of the two ferromagnets diminish with increasing D_N, and therefore the pair correlations become less sensitive to variations in ϕ_1', as observed for the largest $D_N = 500$ case. Other than

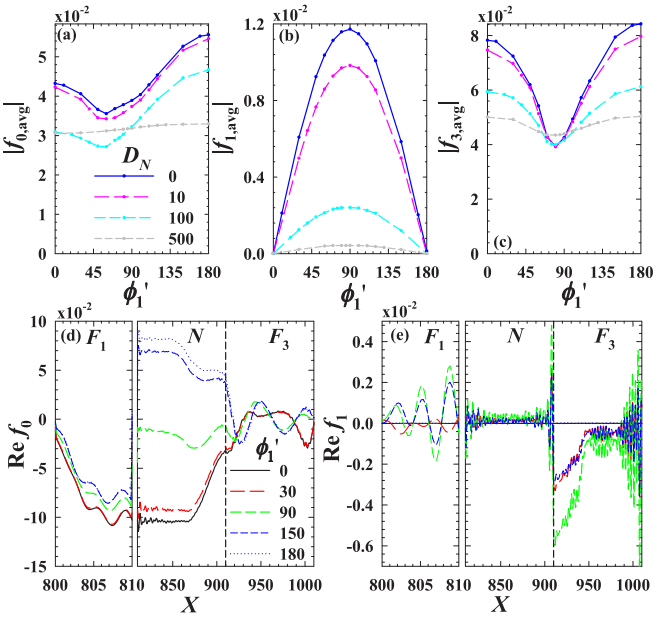

FIG. 10. (Color online) Top row, panels (a)–(c): Normalized singlet and triplet correlations versus in-plane relative magnetization angle $\phi_1' \equiv \phi_1 + 90^\circ$ for a SF_1NF_3S structure. The magnitudes of these pair correlations are averaged over the F_3 region. The geometrical and material parameters are the same as in Fig. 6(b). The bottom panels (d) and (e) correspond to the local spatial behavior of the triplet correlations for the $D_N = 100$ case studied in the top panels. The two F regions are plotted in separate frames to discern the triplet correlations in the narrow F_1 region. The dashed vertical lines represent the interface between the N and F_3 regions. Several values of ϕ_1' are considered, as shown in the legend.

the diminished magnitudes, the overall trends and behavior, however, do not depend strongly on the presence of the normal-metal spacer. This may be important in experiment design, where spacers are often needed. The opposite-spin triplet correlations f_0 and the singlet pair amplitude ($f_3 \equiv \Delta/g$) in Figs. 10(a) and 10(c) behave in rather similar ways, but f_3 is more symmetric about the orthogonal direction $\phi_1' = 90^\circ$. When the relative magnetization orientation varies in inhomogeneous S/F systems, the process of singlet-triplet conversion plays a role in the transport and thermodynamic properties of such systems. It is apparent from Figs. 10(a) and 10(b) that the orientation ϕ_1' that leads to a minimum in f_0 and f_3 corresponds to that where f_1 is largest. These occurrences arise when the exchange fields in F_1 and F_3 are nearly orthogonal. This angle for f_0 slightly shifts with variations in D_N. Changing D_N is seen to cause the optimal angle for local minima or maxima to differ from the expected $\pi/2$ result. The exact angle for this can only be determined from a numerical self-consistent calculation as done here.

In Figs. 10(d) and 10(e) we display the spatial dependence of the real components of the triplet correlations throughout each of the three junction regions discussed in the top panels. Results for five different relative magnetic orientations are presented (see legend). Considering first Fig. 10(d) in the F_1 region, we see behavior similar to that found for the wider junction case in Fig. 9, including a relatively weak dependence on the orientation angle ϕ_1' (as opposed to the phase difference $\Delta\varphi$). The central N region is most affected by variations in ϕ_1': the real part of f_0 changes sign when ϕ_1' is swept from the P to AP state, and nearly vanishes altogether at $\phi_1' \approx 90^\circ$. In F_3, a series of oscillations emerge with a periodicity similar to that found in Fig. 9 since an exchange field of the same strength was used. In Fig. 10(e), the equal-spin f_1 amplitudes exhibit considerably different behavior. First, only three of the considered ϕ_1' yield nonzero results since the P and AP configurations cannot generate equal-spin triplet correlations. Interestingly, within the F_1 region f_1 does not exhibit a slow decay, but rather oscillates with a period that is much shorter than the oscillation period of opposite spin pairs governed by spin-up and -down wave vectors. We find that within the normal-metal layer, there is nearly a complete absence of equal-spin correlations, this is accompanied by the appearance of opposite-spin correlations f_0 [see Fig. 10(d)]. The f_1 amplitudes are largest in the F_3 layer, for the relative orientation of $\phi_1' = 90^\circ$, in agreement with the averaged results in Fig. 10(b). For the relative magnetization angles of $\phi_1' = 30^\circ$ and $\phi_1' = 150^\circ$, the f_1' amplitudes are identical due to the symmetry about $\phi_1' = 90^\circ$. One can now correlate the features Figs. 9 and 10 to Fig. 4. From Fig. 4, we learn that the N magnetic configuration often leads to the appearance of π-Josephson junctions. From the behavior of the charge current in Fig. 6(b), we see that J_x vanishes at ϕ_1' where the averaged opposite-spin singlet and triplet correlations are smallest and when f_1 is largest. Here, we are able to give concrete proof that in the N cases the average magnitude of equal-spin triplet correlations are maximized and weakly dependent on $\Delta\varphi$. Therefore, the CPRs for different magnetic configurations are essentially characterized by their detailed singlet/triplet nature.

We next examine, in Fig. 11, the behavior of the averaged triplet and singlet amplitudes, as the magnetic orientation angles θ_2 (top panels) and ϕ_1' (bottom panels) are changed, in more complicated $SF_1F_2F_3S$ Josephson junctions. This study is therefore complementary to the results shown in Fig. 7 involving the charge supercurrent. The geometric parameters are $D_{F_1} = D_{F_2} = 10$ and $D_{F_3} = 100$. The region in which the pair correlations are averaged over is specified in the top legends. In the top row of Fig. 11 we present results for magnetization orientations θ_2 sweeping the entire angular range from 0° to 360°, while the magnetizations are aligned along z in F_1 and along y in F_3. Therefore, when $\theta_2 = 0^\circ$ or 180°, all three ferromagnets have mutually orthogonal magnetizations, corresponding to a high degree of magnetic inhomogeneity. Under these circumstances, one can expect that the equal-spin triplet correlations f_1 should be, on the average, at their highest values, while the opposite spin correlations should be weakest. Indeed, in the central region F_2, the opposite-spin singlet f_3 and triplet f_0 correlations possess minima near these angles, in contrast to the spatially averaged f_1 amplitudes, which peak at those orientations. Although the general trends are usually the same for all F layers, geometrical effects can result in self-consistent triplet correlations with more intricate nontrivial structure, and this is the case with the averages over the F_1 and F_3 regions where the proximity effects are most prominent. In the bottom panels of Fig. 11, we consider in-plane magnetization rotations of the F_1 layer. The other ferromagnets F_2 and F_3 have their

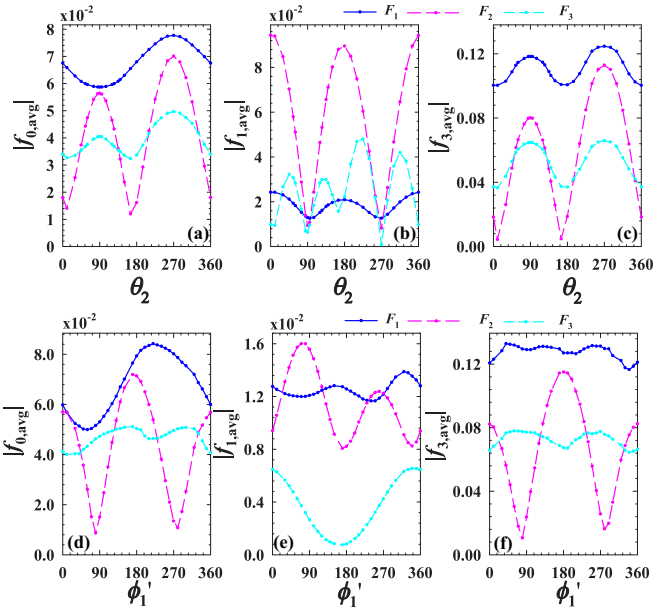

FIG. 11. (Color online) Normalized triplet $|f_{0,\mathrm{avg}}|$, $|f_{1,\mathrm{avg}}|$, and singlet $|f_{3,\mathrm{avg}}|$ amplitudes, averaged over the F regions indicated on the overhead legends, plotted as functions of θ_2 and ϕ_1'. The geometrical and material parameters correspond to the $D_{F_3} = 100$ cases presented in Fig. 7.

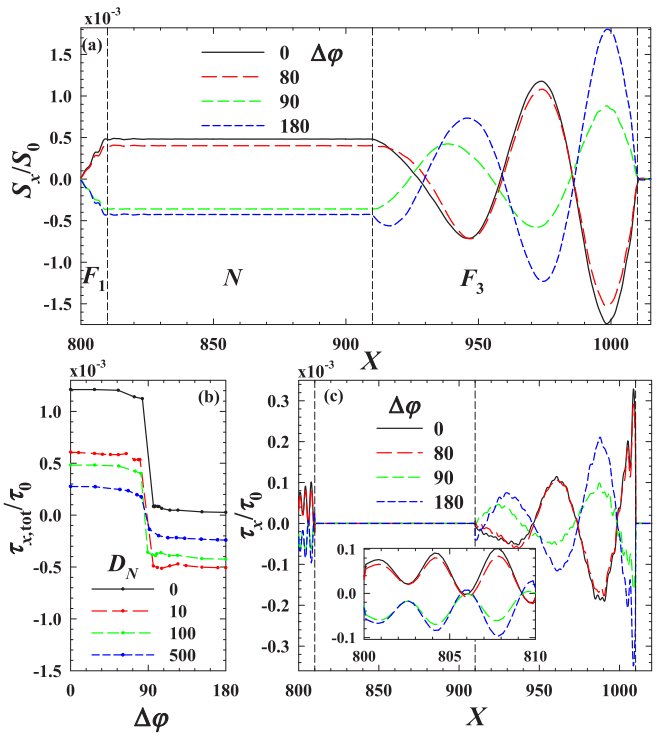

FIG. 12. (Color online) (a) Normalized x component of the spin current in an SF_1NF_3S Josephson junction vs position. The geometric widths are $D_{F_1} = 10$, $D_{F_2} = 100$, and $D_N = 100$. There is moderate interface scattering with $H_B = 0.5$ [see, e.g., Fig. 4(a)]. The dashed vertical lines mark the interfaces. (b) The total torque $\tau_{x,\mathrm{tot}}$ acting within the F_1 region as a function of $\Delta\varphi$. Several normal-metal widths are considered (see legend). The $D_N = 0$ case has been shifted downwards by 4×10^{-3} for comparison purposes. In (c), the x component of the local torque is shown vs position with the same phase differences used in (a). The inset is a magnification of the torque within the narrow F_1 region ($800 < X < 810$).

magnetizations fixed in the y and z directions, respectively. For this situation, the opposite-spin f_0 amplitudes in F_1 are seen to be 2π periodic, peaking at $\phi_1' \approx 225°$. As in the previous case, there are simple correlations between the maximum and minimum values of f_0 and f_1 in F_2. These triplet amplitudes are seen to be largest when the relative orientations between F_1 and F_2 are either P ($\phi_1' = 0°, 360°$) or AP ($\phi_1' = 180°$). This is consistent with the behavior of the triplet amplitudes found in double-magnet spin valve systems [38].

D. Spin transport

Having established the salient features of supercurrent charge transport and pair correlations in a variety of ferromagnetic Josephson junctions, we now explore the spin degree of freedom and determine the crucial spin currents and the associated STT. The current that is generated from the macroscopic phase differences between the S electrodes can become spin polarized [13,49] when entering one of the ferromagnetic regions. This spin current can then interact with the other ferromagnets and be modified by the local magnetizations due to the spin-exchange interaction, via the existence of STT. The conservation law associated with this process is described by Eqs. (28) and (29). It is important not only to understand the behavior of the spin-polarized currents in ferromagnetic Josephson junctions, but also the various ways in which to manipulate them for practical spintronic applications. With the insertion of N layers, the anisotropy energies between the magnetization of one of the F layers, typically pinned by an antiferromagnet, and that of a "free" F layer can be overcome via, e.g., a small external field [19]. As stated in Ref. [49], the STT can be studied through the effect of the Josephson induced exchange interaction provided that the interaction energy exceeds the anisotropy energy. We therefore investigate from a microscopic and self-consistent perspective the equilibrium spin currents and associated torques throughout the entire junction regions as functions of position, phase difference, and magnetization orientation angles.

In Fig. 12(a), we consider the spatial dependence of the spin current in a SF_1NF_3S junction. The geometrical parameters used in this plot are the same as in Fig. 4(a), with $D_N = 100$. Our geometry ensures that the generally tensorial spin current is reduced to a vector in spin space, representing a spin vector current flowing in the spatial x direction and having in general three components in spin space. We display the spatial dependence of the x spin component S_x (normalized as previously discussed). Because the exchange interaction (and hence the torque) vanishes in the N and S regions, only the F regions of the junction can have a spatially varying spin current: in the N and S regions the spin current must be spatially invariant. Under our constant-phase and zero-voltage boundary conditions, the outer s-wave superconducting regions do not [38] support a spin current, and hence $\boldsymbol{S}$ vanishes there. The central nonmagnetic N layer, however, couples the two ferromagnets via a constant spin current, which is related

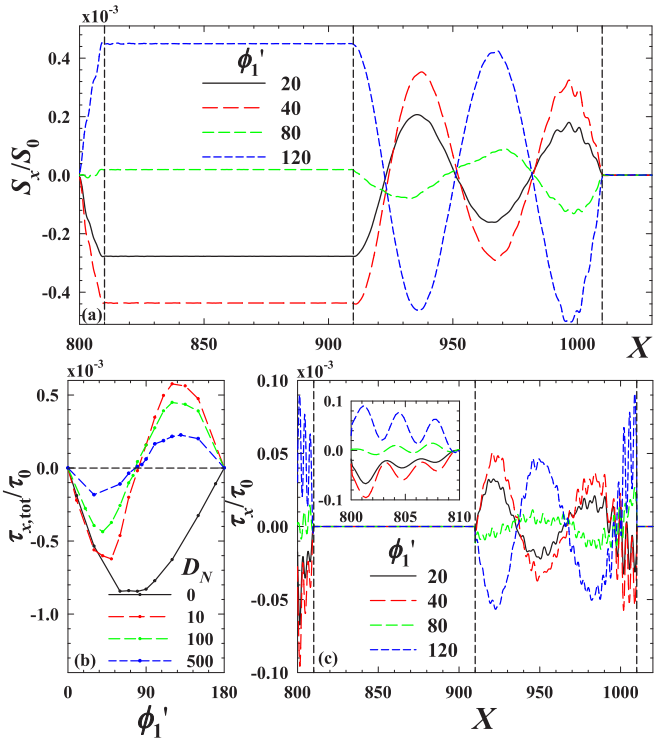

FIG. 13. (Color online) (a) Normalized spin current in an SF_1NF_3S Josephson junction as a function of position. The geometric widths are $D_{F_1} = 10$, $D_{F_2} = 100$, and $D_N = 100$. The interface scattering strength is set to $H_B = 0.8$. These values are the same as in Fig. 6(b). The dashed vertical lines mark the interfaces. (b) Illustrates the total torque $\tau_{x,\mathrm{tot}}$ within the F_1 region as a function of the relative in-plane magnetization angle ϕ_1'. Several normal-metal widths are considered as depicted in the legend. The $D_N = 0$ results have been multiplied by $\frac{1}{5}$ for comparison purposes. In panel (c) the x component of the torque is shown as a function of position for the same case considered in (a).

to the net torque acting within the F regions [see Eq. (30)]. The spin current oscillates in the F_3 region. The amplitude of these oscillations depends on $\Delta\varphi$, while the period does not: the points in F_3 where S_x vanish are independent of $\Delta\varphi$. If a ferromagnet is very thin, as occurs for F_1, the spin currents vary nearly linearly with X, which can be viewed as a small segment of a sinusoidal function. To present an overall view of how the change in spin current and its associated torque vary as the phase varies, we do this in terms of the total torque, defined as the integral of the local torque, normalized as discussed above, over dimensionless distance. We plot in Fig. 13(b) the total torque $\tau_{x,\mathrm{tot}}$ within F_1 for a few values of the interlayer N spacer thickness. In all cases, $\tau_{x,\mathrm{tot}}$ is relatively uniform until a sharp crossover near $\Delta\varphi = 90^\circ$, where the net torque changes sign, coinciding with the point of supercurrent reversal [Fig. 4(a)]. Interestingly, only when the normal-metal insert is present does $\tau_{x,\mathrm{tot}}$ reverse direction. Figure 13(c) illustrates the local x component of the torque τ_x as a function of position throughout the entire junction region. The inset is the same quantity, but plotted only over the narrow F_1 region. To correlate with Fig. 13(a), the $D_N = 100$ case is considered here. Each curve represents a different phase difference as shown in the legend for Fig. 13(a). For in-plane exchange field interactions, no other component of the torque can exist in equilibrium when spin currents do not enter or leave the superconducting electrodes [49]. Thus, the net torque for the entire system must vanish, requiring $\tau_{x,\mathrm{tot}}$ for each of the two F regions to be opposite in sign, despite the dissimilar spatial behavior as exhibited in Fig. 13(c). Comparing Figs. 13(a) and 13(c), it is also evident that within the oscillatory F_3 region, τ_x and S_x behave similarly, but are out of phase by approximately 90°, in agreement with Eq. (29). Since the spin current was shown to be uniform in the normal-metal region, the torque is seen to vanish there, as it should be in regions where the magnetic exchange interaction is absent.

We next study how the spin currents and associated torques change when varying the relative exchange field directions between F_1 and F_3 in an SF_1NF_3S junction. A supercurrent is generated in the structure by maintaining a phase difference which we take to be $\Delta\varphi = 100^\circ$ in Fig. 13. We rotate in-plane magnetization F_1, while keep that in F_3 fixed along the y [as in Fig. 6(b)]. Control of the free-layer magnetization can be achieved experimentally via external magnetic fields [19] or spin-torque switching [64,65]. In Fig. 13(a), the x component of the local spin current S_x is shown throughout the junction as a function of position X, for four values of the ϕ_1' angle (we have $\theta_1 = \theta_2 = 90^\circ$). The spin current is again seen to be a nonconserved quantity within the ferromagnets, reflecting the existence of a STT. In the nonmagnetic normal metal connecting the two F regions, the current is constant, and its value as ϕ_1' is varied S_x cycles from positive to negative. To explore this further, we examine the total change in spin current across F_1, as ϕ_1' sweeps from the P to AP state. This change is related via Eq. (30) to the integrated torque in this region. Hence, in Fig. 13(b) we plot $\tau_{x,\mathrm{tot}}$ versus ϕ_1' for a wide range of D_N. When the normal metal is absent ($D_N = 0$), the magnitude of the total torque reaches its peak around $\phi_1' = 90^\circ$, indicating that this component of the torque, which tends to align the magnetic moments of the two F layers is largest when they are mutually orthogonal. This makes sense physically. The presence of even a thin normal-metal spacer causes $\tau_{x,\mathrm{tot}}$ to become much smaller (the $D_N = 0$ results are plotted after dividing them by five) and nearly π symmetric, so that now the orthogonal magnetic configuration produces negligible net torque within the F layers. Increasing D_N reduces the ferromagnetic coupling and hence reduces the magnitude of the mutual torques, although the π periodicity is retained. Finally, in Fig. 13(c) we plot the local value of the torque, and find its spatial behavior to be consistent with that of S_x as given in Eq. (29).

Finally, we consider the $SF_1F_2F_3S$ system, studied previously in Fig. 7(a), with $D_{F_1} = D_{F_2} = 10$ and $D_{F_3} = 100$. A phase difference of $\Delta\varphi = 100^\circ$ maintains a constant current throughout the junction, and there is moderate interface scattering, with $H_B = 0.8$. The magnetization in F_1 is along z, and in F_3, it is along y. The central ferromagnet F_2 has a magnetization vector that is rotated the xz plane (see Fig. 1), so that for $\theta = 0^\circ$, it is oriented along x, and for $\theta = 90^\circ$, it is aligned along z. For these more complex magnetic configurations, where one of the F layers possesses an out-of-plane exchange field, all three spin components of the current $\boldsymbol{S}$ must be considered. The top panels in Fig. 14 depict the components of the total torque $\tau_{i,\mathrm{tot}}$ ($i = x,y,z$) for

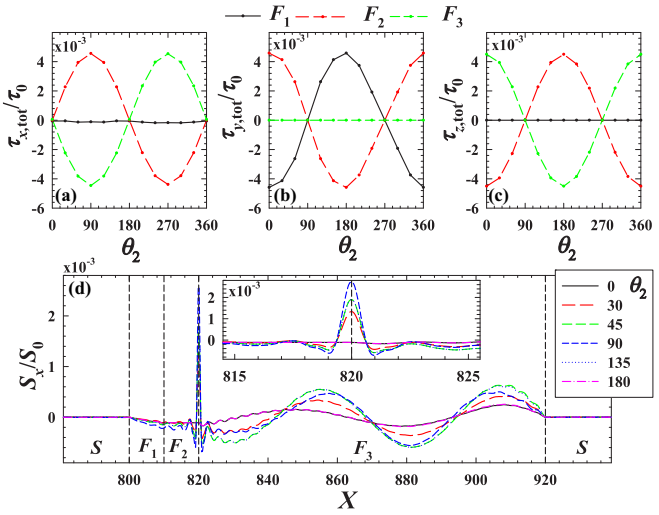

FIG. 14. (Color online) Top panels: total torque within each of the ferromagnet regions (see overhead legend) in an $SF_1F_2F_3S$ junction as the angle θ_2 varies. The system parameters are those used in Fig. 7(a). The sum $\tau_{i,\mathrm{tot}}$ $(i = x,y,x)$ over all three ferromagnetic regions vanishes for each component. In the bottom panel, the spatial behavior of the normalized x component of the spin current is shown throughout the system for a few select magnetization orientations θ_2 (see legend). The inset is a magnification of the region centered around the F_2/F_3 interface located at $X = 820$. Vertical dashed lines in the main plot mark interface locations.

each ferromagnet region, identified in the legend above these panels. Since the total torque in a given direction equals [see Eq. (30)] the overall change in spin current, and, as explained above there is no spin current in the S regions at fixed phase, the sum of each component $\tau_{i,\mathrm{tot}}$ over all F regions must be zero. This is seen in these three panels, where the oscillatory curves exactly cancel one another. For each of the three components, we also observe that the total torque in either F_1 or F_3 nearly vanishes over the whole angular range of θ_2. This follows from the expression for the local torque (21), which implies that $\boldsymbol{\tau}$ is orthogonal to the exchange field vector $\boldsymbol{h}$, and the magnetization $\boldsymbol{m}$. For example, considering the leftmost panel the only component of the exchange field in F_1 is along z, and since $\tau_x \sim m_y h_z$, a y component of the magnetization is needed in F_1 to generate a torque along x. However, $\boldsymbol{h}$ in the adjacent F_2 rotates solely in the xz plane, and thus m_y vanishes in F_1 except in a narrow region near the interface (see Ref. [38]) resulting in a very small value for the averaged $\tau_{x,\mathrm{tot}}$.

When the spin current density $\boldsymbol{S}$ is spatially nonuniform, the resulting torque influences the magnetization configurations. It is therefore insightful to examine also in this case, as we did in Figs. 12 and 13, the spatial behavior of the spin current. The results are displayed in the bottom panel of Fig. 14. For clarity, we present only the x component S_x since the other spin components behave similarly. A few representative angle orientations θ_2 are considered (see legend). As expected, we see that S_x vanishes in the outer S electrodes. Within the larger F_3 region, the spin current undergoes regular oscillations which are much harder to distinguish in the narrow F_2 and F_1 regions. To compare with the previous results, we see from this panel that the change in the x component of the spin current ΔS_x across the F_1 boundaries is negligible, in agreement with the results in the left top row panel. In F_2, this component of the current is very small near the left interface, but it increases near the right edge, so that ΔS_x agrees well with the $\tau_{x,\mathrm{tot}}$ variations in F_2 observed in the left top panel. Also in agreement is the enhancement of the spin current S_x that is narrowly peaked at the F_2/F_3 interface for θ_2 that are near normal to the plane ($\theta_2 \approx 90^\circ$). Finally, since the interface adjoining F_3 and the right S electrode has $S_x = 0$, the change ΔS_x in the F_3 region is due entirely from the value of the spin current at the F_2/F_3 interface, thus resulting in ΔS_x that is exactly opposite to that in F_2.

IV. CONCLUSIONS

We have presented here an extensive study of the Josephson currents flowing in generic ballistic structures of the *SFS* type where the F regions contain two or three ferromagnetic layers, possibly separated by normal spacers. For the *SFFS*-type spin valves, we study their transport properties by considering different in-plane relative magnetization angles. When the third F layer is present (*SFFFS*), we allow the central F region to have out-of-plane magnetic orientation while those for the two outer F layers are still in plane. Our self-consistent formalism ensures [38] that the charge conservation law is satisfied and that the proper relations that balance the STTs and the gradients of the spin current components hold. Results are given for a wide range of values of the geometrical and orientation parameters, as well as interfacial scattering.

We have organized our results in several sections. We first have considered (Sec. III A) the current-phase relations (CPRs) as a function of geometrical parameters (layer thicknesses) at fixed relative angles between the in-plane magnetizations: parallel (P), antiparallel (AP), and normal (N). We find that, in general, larger geometric asymmetry (the aspect ratio for the thicknesses of the two outer F layers) leads to larger superharmonic (π periodic) behavior. This is particularly pronounced in the two-magnet case. It is found that the strength of interfacial scattering can affect the magnitude of the critical current. Next, in Sec. III B, we consider the effect of magnetization misorientation on the CPR. We find that these effects are profound. In particular, by sweeping the relative in-plane angle from P to AP at fixed phase differences $\Delta\varphi$ between two S electrodes, the supercurrent flow first vanishes at N configurations, followed by reversal of its direction. These can be understood to a very large extent by noting that the generation of induced spin triplets (studied in Sec. III C) is correlated with magnetic inhomogeneity and, via this phenomenon, to the CPR relationships. In Sec. III C, we also presented the local spatial behavior of both the $m = 0$ and ± 1 triplet correlations and carefully quantify each component as functions of magnetic orientations and $\Delta\varphi$. The results clearly demonstrate the existence of the singlet-to-triplet conversion in the Josephson junctions. Finally, in Sec. III D we have discussed spin transport and shown that, due to the interaction between the charge current and the magnetizations, both the spin current and the STT oscillate in the F regions. By varing $\Delta\varphi$ or the magnetic misalignment angles, the phase of their oscillations can change accordingly. In addition, we have shown how the spin current gradient equals the STT.

We hope that our rather comprehensive study of transport in these multilayer structures will guide the experimentalist in choosing optimal configurations for building devices such as low dissipation memory storage units, which are expected to rely on the behavior of the Josephson junctions studied here. Based on our investigation, the flow direction of charge supercurrents can be controlled by varying the relative orientation angles in *SFFS* and *SFFFS clean* heterostructures. This property renders these systems prominent candidates in making superconducting spin valves. Experimentally, these switching effects can be easily achieved by applying an external magnetic field [18,19]. Our study indicates that by adjusting the layer thicknesses can lead to a modified behavior of the CPR. In particular, we urge experimentalists to consider ferromagnets with asymmetric widths while making such spin valves in order to maximize the switching effects.

ACKNOWLEDGMENTS

K.H. was supported in part by IARPA and ONR. K.H. was also supported in part by a grant from the Department of Defense High Performance Computing Modernization Program. K.H. would like to thank M. Alidoust for helpful discussions. In the latest stages of this work, O.T.V. was supported in part by DOE Grant No. DE-SC0014467.

APPENDIX A: NUMERICAL PROCEDURE

Here, we discuss some technical aspects of the numerical procedure used in calculating the spin and charge currents governed by the Andreev bound states. We first expand [29] the quasiparticle amplitudes in terms of a complete set:

$$\psi_n(x) = \sqrt{\frac{2}{d}} \sum_{q=0}^{N} \sin(k_q x)\hat{\psi}_q(k_q), \tag{A1}$$

where we use the shorthand notation $\psi_n(x) = [u_{n\uparrow}(x), u_{n\downarrow}(x), v_{n\uparrow}(x), v_{n\downarrow}(x)]$, and $\hat{\psi}_q = (\hat{u}_{q\uparrow}, \hat{u}_{q\downarrow}, \hat{v}_{q\uparrow}, \hat{v}_{q\downarrow})$. We write the wave-vector index as $k_q = q\pi/d$, so that $\Delta k_q \equiv k_{q+1} - k_q = \pi/d$. Thus, N grid points subdivide the system of width d. We take d to be large enough so that the results become independent of d. The next step involves Fourier transforming the real-space BdG equations [Eq. (4)], resulting in the following set of coupled equations in momentum space:

$$\begin{pmatrix} \hat{H}_0 - \hat{h}_z & -\hat{h}_x + i\hat{h}_y & 0 & \hat{\Delta} \\ -\hat{h}_x - i\hat{h}_y & \hat{H}_0 + h_z & \hat{\Delta} & 0 \\ 0 & \hat{\Delta}^* & -(\hat{H}_0 - \hat{h}_z) & -\hat{h}_x - i\hat{h}_y \\ \hat{\Delta}^* & 0 & -\hat{h}_x + i\hat{h}_y & -(\hat{H}_0 + \hat{h}_z) \end{pmatrix} \begin{pmatrix} \hat{u}_\uparrow \\ \hat{u}_\downarrow \\ \hat{v}_\uparrow \\ \hat{v}_\downarrow \end{pmatrix}$$

$$= \epsilon_n \begin{pmatrix} \hat{u}_\uparrow \\ \hat{u}_\downarrow \\ \hat{v}_\uparrow \\ \hat{v}_\downarrow \end{pmatrix}. \tag{A2}$$

Here, we have defined $\hat{u}_\sigma = (\hat{u}_{1\sigma}, \hat{u}_{2\sigma}, \ldots, \hat{u}_{N\sigma})$, $\hat{v}_\sigma = (\hat{v}_{1\sigma}, \hat{v}_{2\sigma}, \ldots, \hat{v}_{N\sigma})$, and the matrix elements

$$\hat{H}_0(q,q') = \frac{2}{d} \int_0^d dx \left(\frac{k_q^2}{2m} + \epsilon_\perp - \mu \right) \sin(k_q x) \sin(k_{q'} x), \tag{A3}$$

$$\hat{\Delta}(q,q') = \frac{2}{d} \int_0^d dx\, \Delta(x) \sin(k_q x) \sin(k_{q'} x), \tag{A4}$$

$$\hat{h}_i(q,q') = \frac{2}{d} \int_0^d dx\, h_i(x) \sin(k_q x) \sin(k_{q'} x), \quad i = x,y,z \tag{A5}$$

where $\epsilon_\perp$ is the kinetic energy on the y-z plane. Our numerical procedure for calculating the supercurrent involves initially assuming a constant amplitude form for the pair potential in each S layer, but with a total phase difference $\Delta\varphi$ ($0, \Delta\varphi$ at each S region). We then expand the pair potential via Eq. (A4). Similarly, the exchange field and free-particle Hamiltonian are expanded using Eqs. (A5) and (A3), respectively. We then find the quasiparticle energies and amplitudes by diagonalizing the resultant momentum-space matrix [Eq. (A2)]. Once the momentum-space wave functions and energies are found, they are transformed back into real-space via Eq. (A1). From them, a new pair potential $\Delta(x)$ is self-consistently determined via Eq. (7) through the entire region except for a small region (three coherence lengths from the sample edges) where the pair potential is fixed to its bulk absolute value, with phases $0, \Delta\varphi$. The newly calculated $\Delta(x)$ is then used in the BdG equations and the above process is repeated iteratively until convergence is achieved. When determining the current-phase relations, $\Delta\varphi$ is defined as the difference in phases between the superconductors in the outermost self-consistent regions.

As self-consistency evolves with each iteration, the final $\Delta\varphi$ often differs slightly from the fixed difference $\Delta\varphi$ that is set in the non-self-consistent regions. Thus, to have $\Delta\varphi$ fixed to a prescribed value while varying other parameters, e.g., θ_2, additional calculations are needed with slightly different initial choices for the phase $\Delta\varphi$. Following the discussion in the main text, when current is flowing through the junction, the self-consistently calculated regions have always been found to possess the necessary spatially constant current. The fixed-phase non-self-consistent edge regions provide the physically necessary source or sink of current, via the applied electrodes, thus acting as an effective boundary condition.

APPENDIX B: SPIN ROTATION MATRICES

Here, we show how to perform the spin rotations for the two triplet components f_0 and f_1 (the singlet amplitude is of course invariant under spin rotations). The problem simplifies if all one wishes is to align the spin quantization axis with the local magnetization direction: this affords easier physical interpretation of the results. The central quantity that we use to perform the desired rotations is the spin transformation matrix $\mathcal{T}$ in particle-hole space. The quasiparticle amplitudes transform as

$$\Psi_n'(x) = \mathcal{T}\Psi_n(x). \tag{B1}$$

In our notation the matrix $\mathcal{T}$ can be written as

$$\mathcal{T} = \begin{bmatrix} \mathcal{A} & 0 \\ 0 & \mathcal{B} \end{bmatrix}, \tag{B2}$$

where the submatrices $\mathcal{A}$ and $\mathcal{B}$ are trigonometric functions solely of the angles that describe the local magnetization orientation. Expressing the orientation of the exchange fields

in the regions F_1 and F_2 in terms of the angles θ_i and ϕ_i introduced in Eq. (6) we can write $\mathcal{A}$ and $\mathcal{B}$ as the following 2×2 matrices:

$$\mathcal{A} = \begin{bmatrix} \cos(\phi_i/2)\sin(\theta_i^+) + i\sin(\phi_i/2)\sin(\theta_i^-) & -\cos(\phi_i/2)\sin(\theta_i^-) - i\sin(\phi_i/2)\sin(\theta_i^+) \\ \cos(\phi_i/2)\sin(\theta_i^-) - i\sin(\phi_i/2)\sin(\theta_i^+) & \cos(\phi_i/2)\sin(\theta_i^+) - i\sin(\phi_i/2)\sin(\theta_i^-) \end{bmatrix}, \tag{B3}$$

$$\mathcal{B} = \begin{bmatrix} \cos(\phi_i/2)\sin(\theta_i^+) - i\sin(\phi_i/2)\sin(\theta_i^-) & \cos(\phi_i/2)\sin(\theta_i^-) - i\sin(\phi_i/2)\sin(\theta_i^+) \\ -\cos(\phi_i/2)\sin(\theta_i^-) - i\sin(\phi_i/2)\sin(\theta_i^+) & \cos(\phi_i/2)\sin(\theta_i^+) + i\sin(\phi_i/2)\sin(\theta_i^-) \end{bmatrix}. \tag{B4}$$

Here, we have defined $\theta_i^{\pm} \equiv \theta_i/2 \pm \pi/4$. Using the spin rotation matrix $\mathcal{T}$, we can transform the original BdG equations $\mathcal{H}\Psi_n = \epsilon_n \Psi_n$ [Eq. (4)] by performing the unitary transformation: $\mathcal{H}' = \mathcal{T}\mathcal{H}\mathcal{T}^{-1}$ (of course, we have $\mathcal{T}^{\dagger}\mathcal{T} = 1$). We then end up with the magnetization effectively along the new z axis and

$$\mathcal{H}' = \begin{pmatrix} \mathcal{H}_0 - h & 0 & 0 & \Delta \\ 0 & \mathcal{H}_0 + h & \Delta & 0 \\ 0 & \Delta^* & -\mathcal{H}_0 + h & 0 \\ \Delta^* & 0 & 0 & -\mathcal{H}_0 - h \end{pmatrix}. \tag{B5}$$

One of the benefits of working in this rotated coordinate system is that now the Hamiltonian matrix can be reduced to a smaller 2×2 size by using symmetry properties that now exist between the quasiparticle amplitudes and energies [29]. As is the case under all unitary transformations, the eigenvalues here are preserved, but the eigenvectors are modified in general according to Eq. (B1). Thus, for example, operating on the wave functions using Eq. (B1), and examining the terms involved in calculating the singlet pair correlations [Eq. (7)], it is easily shown that for a given set of quantum numbers n and position x, the following relation between the transformed (primed) and untransformed quantities holds: $u'_{n\uparrow}v'^*_{n\downarrow} + u'_{n\downarrow}v'^*_{n\uparrow} = u_{n\uparrow}v^*_{n\downarrow} + u_{n\downarrow}v^*_{n\uparrow}$. Thus, the terms that dictate the singlet pairing are invariant for any choice of quantization axis, transforming as scalars under spin rotations, as they should.

The terms governing the triplet amplitudes on the other hand are generally not invariant under the spin rotation. It is illuminating to see how both the equal-spin and different-spin triplet correlations transform. The relevant particle-hole products in Eq. (9) that determine f_0 upon the spin transformations obey the following relationships:

$$u'_{n\uparrow}v'^*_{n\downarrow} - u'_{n\downarrow}v'^*_{n\uparrow} = \cos\theta_i(u_{n\uparrow}v^*_{n\uparrow} + u_{n\downarrow}v^*_{n\downarrow}) + \sin\theta_i[\cos\phi_i(u_{n\uparrow}v^*_{n\downarrow} - u_{n\downarrow}v^*_{n\uparrow}) + i\sin\phi_i(u_{n\uparrow}v^*_{n\uparrow} - u_{n\downarrow}v^*_{n\downarrow})]. \tag{B6}$$

Similarly, the quasiparticle terms in the sum for f_1 [Eq. (10)] transform as

$$u'_{n\uparrow}v'^*_{n\uparrow} + u'_{n\downarrow}v'^*_{n\downarrow} = \sin\theta_i(u_{n\uparrow}v^*_{n\uparrow} + u_{n\downarrow}v^*_{n\downarrow}) + \cos\theta_i[\cos\phi_i(u_{n\downarrow}v^*_{n\uparrow} - u_{n\uparrow}v^*_{n\downarrow}) + i\sin\phi_i(u_{n\downarrow}v^*_{n\downarrow} - u_{n\uparrow}v^*_{n\uparrow})]. \tag{B7}$$

Thus, the triplet amplitudes f_0 and f_1 in the rotated system are linear combinations of the f_1 and f_0 in the original unprimed system (and vice versa). It is a simple matter to go from the rotated to the original system (and vice versa) by the route expressed in Eq. (B1).

[1] M. Eschrig, Phys. Today **64**(1), 43 (2011).
[2] S. Hikino and S. Yunoki, Phys. Rev. Lett. **110**, 237003 (2013).
[3] R. Grein, M. Eschrig, G. Metalidis, and G. Schön, Phys. Rev. Lett. **102**, 227005 (2009).
[4] A. A. Golubov, M. Yu. Kupriyanov, and E. ll'ichev, Rev. Mod. Phys. **76**, 411 (2004).
[5] M. Alidoust and K. Halterman, Phys. Rev. B **89**, 195111 (2014).
[6] K. Halterman and O. T. Valls, Phys. Rev. B **70**, 104516 (2004).
[7] K. Halterman and O. T. Valls, Phys. Rev. B **69**, 014517 (2004).
[8] V. V. Ryazanov, V. A. Oboznov, A. Yu. Rusanov, A. V. Veretennikov, A. A. Golubov, and J. Aarts, Phys. Rev. Lett. **86**, 2427 (2001).
[9] Z. Pajović, M. Božović, Z. Radović, J. Cayssol, and A. Buzdin, Phys. Rev. B **74**, 184509 (2006).
[10] T. E. Baker, A. Richie-Halford, and A. Bill, New J. Phys. **16**, 093048 (2014).
[11] F. S. Bergeret, A. F. Volkov, and K. B. Efetov, Phys. Rev. B **64**, 134506 (2001).
[12] L. Trifunovic, Z. Popović, and Z. Radović, Phys. Rev. B **84**, 064511 (2011).
[13] Z. Shomali, M. Zareyan, and W. Belzig, New J. Phys. **13**, 083033 (2011).
[14] K. Halterman, P. H. Barsic, and O. T. Valls, Phys. Rev. Lett. **99**, 127002 (2007).
[15] A. Singh, S. Voltan, K. Lahabi, and J. Aarts, Phys. Rev. X **5**, 021019 (2015).
[16] M. Eschrig, J. Kopu, J. C. Cuevas, and G. Schön, Phys. Rev. Lett. **90**, 137003 (2003).
[17] A. I. Buzdin, Rev. Mod. Phys. **77**, 935 (2005).
[18] X. L. Wang, A. Di Bernardo, N. Banerjee, A. Wells, F. S. Bergeret, M. G. Blamire, and J. W. A. Robinson, Phys. Rev. B **89**, 140508 (2014).
[19] A. A. Jara, C. Safranski, I. N. Krivorotov, C.-T. Wu, A. N. Malmi-Kakkada, O. T. Valls, and K. Halterman, Phys. Rev. B **89**, 184502 (2014).
[20] F. Chiodi, J. D. S. Witt, R. G. J. Smits, L. Qu, G. B. Halász, C.-T. Wu, O. T. Valls, K. Halterman, J. W. A. Robinson, and M. G. Blamire, Europhys. Lett. **101**, 37002 (2013).
[21] P. G. de Gennes, *Superconductivity of Metals and Alloys* (Addison-Wesley, Reading, MA, 1989).
[22] M. Zareyan, W. Belzig, and Yu. V. Nazarov, Phys. Rev. Lett. **86**, 308 (2001).
[23] A. I. Buzdin, L. N. Bulaevskii, and S. V. Panyukov, Pis'ma Zh. Eksp. Teor. Fiz. **35**, 147 (1982) [JETP Lett. **35**, 178 (1982)].

[24] A. I. Buzdin and M. Y. Kuprianov, Pis'ma Zh. Eksp. Teor. Fiz. **53**, 308 (1991) [JETP Lett. **53**, 321 (1991)].
[25] E. A. Demler, G. B. Arnold, and M. R. Beasley, Phys. Rev. B **55**, 15174 (1997).
[26] J. W. A. Robinson, S. Piano, G. Burnell, C. Bell, and M. G. Blamire, Phys. Rev. Lett. **97**, 177003 (2006).
[27] I. B. Sperstad, J. Linder, and A. Sudbø, Phys. Rev. B **78**, 104509 (2008).
[28] K. Halterman and O. T. Valls, Phys. Rev. B **65**, 014509 (2001).
[29] K. Halterman and O. T. Valls, Phys. Rev. B **66**, 224516 (2002).
[30] F. S. Bergeret, A. F. Volkov, and K. B. Efetov, Phys. Rev. Lett. **86**, 3140 (2001); Phys. Rev. B **68**, 064513 (2003); Rev. Mod. Phys. **77**, 1321 (2005).
[31] K. Halterman, O. T. Valls, and P. H. Barsic, Phys. Rev. B **77**, 174511 (2008).
[32] M. Alidoust, J. Linder, G. Rashedi, T. Yokoyama, and A. Sudbø, Phys. Rev. B **81**, 014512 (2010).
[33] M. Alidoust and K. Halterman, J. Appl. Phys. **117**, 123906 (2015).
[34] J. W. A. Robinson, J. D. S. Witt, and M. G. Blamire, Science **329**, 59 (2010).
[35] T. S. Khaire, M. A. Khasawneh, W. P. Pratt, Jr., and N. O. Birge, Phys. Rev. Lett. **104**, 137002 (2010).
[36] E. C. Gingrich, P. Quarterman, Y. Wang, R. Loloee, W. P. Pratt, Jr., and N. O. Birge, Phys. Rev. B **86**, 224506 (2012).
[37] A. F. Volkov and K. B. Efetov, Phys. Rev. B **81**, 144522 (2010).
[38] C.-T. Wu, O. T. Valls, and K. Halterman, Phys. Rev. B **90**, 054523 (2014).
[39] C. Richard, M. Houzet, and J. S. Meyer, Phys. Rev. Lett. **110**, 217004 (2013).
[40] M. Houzet and A. I. Buzdin, Phys. Rev. B **76**, 060504 (2007).
[41] E. Goldobin, D. Koelle, R. Kleiner, and A. Buzdin, Phys. Rev. B **76**, 224523 (2007).
[42] A. Buzdin, Phys. Rev. B **72**, 100501(R) (2005); M. Houzet, V. Vinokur, and F. Pistolesi, *ibid.* **72**, 220506(R) (2005).
[43] G. Mohammadkhani and M. Zareyan, Phys. Rev. B **73**, 134503 (2006).
[44] Z. Radovic, L. Dobrosavljevic-Grujic, and B. Vujicic, Phys. Rev. B **63**, 214512 (2001); T. T. Heikkila, F. K. Wilhelm, and G. Schon, Europhys. Lett. **51**, 434 (2000).
[45] J. J. A. Baselmans, T. T. Heikkila, B. J. van Wees, and T. M. Klapwijk, Phys. Rev. Lett. **89**, 207002 (2002).
[46] J. Linder and K. Halterman, Phys. Rev. B **90**, 104502 (2014).
[47] A. Pal, Z. H. Barber, J. W. A. Robinson, and M. G. Blamire, Nat. Commun. **5**, 3340 (2014).
[48] E. Zhao and J. A. Sauls, Phys. Rev. B **78**, 174511 (2008).
[49] X. Waintal and P. W. Brouwer, Phys. Rev. B **65**, 054407 (2002).
[50] J.-F. Liu and K. S. Chan, Phys. Rev. B **82**, 184533 (2010).
[51] R. A. Riedel, L.-F. Chang, and P. F. Bagwell, Phys. Rev. B **54**, 16082 (1996).
[52] J. Linder, T. Yokoyama, and A. Sudbø, Phys. Rev. B **77**, 174514 (2008).
[53] C-T. Wu, O. T. Valls, and K. Halterman, Phys. Rev. B **86**, 184517 (2012).
[54] J. B. Ketterson and S. N. Song, *Superconductivity* (Cambridge University Press, Cambridge, UK, 1999).
[55] V. L. Berezinskii, Pis'ma Zh. Eksp. Teor. Fiz. **20**, 628 (1974) [JETP Lett. **20**, 287 (1974)] .
[56] G. Baym and L. P. Kadanoff, Phys. Rev. **124**, 287 (1961).
[57] F. Sols and J. Ferrer, Phys. Rev. B **49**, 15913 (1994).
[58] M. J. M. de Jong and C. W. J. Beenakker, Phys. Rev. Lett. **74**, 1657 (1995); C. W. J. Beenakker, Lect. Notes Phys. **667**, 131 (2005).
[59] C. W. J. Beenakker, Phys. Rev. Lett. **97**, 067007 (2006).
[60] Z. Radovic, N. Lazarides, and N. Flytzanis, Phys. Rev. B **68**, 014501 (2003).
[61] M. Bozovic and Z. Radovic, Phys. Rev. B **71**, 229901(E) (2005).
[62] The Roman "N" in this paper denotes the type of magnetic configuration and is not to be confused with the Italic "*N*" that represents normal metallic layer.
[63] L. Trifunovic, Phys. Rev. Lett. **107**, 047001 (2011).
[64] G. E. W. Bauer, E. Saitoh, and B. J. van Wees, Nat. Mater. **11**, 391 (2012).
[65] A. Brataas, A. D. Kent, and H. Ohno, Nat. Mater. **11**, 372 (2012).